

UNCLASSIFIED



Australian Government
Department of Defence
Defence Science and
Technology Organisation

High Grazing Angle Sea-Clutter Literature Review

Luke Rosenberg¹ and Simon Watts²

1. Electronic Warfare and Radar Division
Defence Science and Technology Organisation

2. C4ISR Division
Thales United Kingdom

DSTO-GD-0736

ABSTRACT

This report reviews the published literature on the characteristics of mono-static radar sea-clutter observed with high grazing angles (typically above about 10°). To date, most of the analysis and modelling of sea-clutter has been undertaken at low grazing angles with the main application being for surface and airborne maritime radars. The report identifies some of the data sets that have been collected and the empirical models that have been developed from them for the normalised radar cross-section. The amplitude statistics and Doppler spectra of high grazing angle clutter are reviewed and the implications for radar design and target detection are discussed.

RELEASE LIMITATION

Approved for public release

UNCLASSIFIED

UNCLASSIFIED

Published by

*Electronic Warfare and Radar Division
DSTO Defence Science and Technology Organisation
PO Box 1500
Edinburgh South Australia 5111 Australia*

*Telephone: (08) 7389 5555
Fax: (08) 7389 6567*

*© Commonwealth of Australia 2013
AR-015-559
March 2013*

APPROVED FOR PUBLIC RELEASE

UNCLASSIFIED

UNCLASSIFIED

High Grazing Angle Sea-Clutter Literature Review

Executive Summary

This report summarises the current literature on high grazing angle sea clutter observed by a mono-static radar. The goal is to assist with the studies being performed by members of the SET-185 panel.

High grazing angles are typically defined to be above 10° . To date, most of the analysis and modelling of sea-clutter has been undertaken at low grazing angles with the main application being for surface and airborne maritime radars. They typically operate at low grazing angles either from necessity or to achieve the best detection performance against small targets. However, there are growing operational requirements to undertake maritime reconnaissance using radar on high-flying air vehicles, especially unmanned aerial vehicles (UAVs). It has therefore become important to better understand the characteristics of sea-clutter at higher grazing angles.

Data collected in this region has unanimously shown a monotonic increase in the mean backscatter with increasing grazing angle. This is due to the increased clutter cell size on the ground which also implies that the amplitude distribution has less variation (i.e. less spiky) than at low grazing angles. However, it has been reported that the amplitude statistics still have significantly non-Gaussian characteristics. The Doppler spectra of sea-clutter is also highly variable, again reflecting the presence of discrete spikes as well as the more dominant Bragg scattering components. When combined together, these factors imply that detection of small targets will become harder as the grazing angle increases.

UNCLASSIFIED

UNCLASSIFIED

This page is intentionally blank

UNCLASSIFIED

Contents

1. INTRODUCTION.....	1
2. BACKGROUND.....	2
2.1 Bragg Resonance Scattering Model	3
2.2 Composite Surface Model	5
2.3 Sea-Spikes	6
2.4 Wind speed, wave height and sea state	7
3. MEASURED DATA SETS.....	8
3.1 Nathanson data.....	9
3.2 NRL 4FR.....	10
3.3 Masuko data.....	11
3.4 MIT Chesapeake bay experiments	12
3.5 TRW Scotland experiments.....	12
3.6 Ingara data.....	13
4. MEAN BACKSCATTER.....	15
4.1 Nathanson models	15
4.1.1 NAAWS model	15
4.1.2 NECAPS model.....	15
4.1.3 TSC model	16
4.1.4 NRL model	16
4.2 Ulaby Models.....	16
4.2.1 Masuko model	17
4.2.2 DSTO IRSG models	20
5. AMPLITUDE DISTRIBUTION.....	22
6. DOPPLER SPECTRA AND CORRELATION	27
6.1 Background	27
6.2 Mean Doppler spectrum models.....	29
6.3 Non-coherent correlation analysis.....	31
6.4 Modelling and simulation of coherent sea-clutter	32
6.4.1 Models.....	32
6.4.2 Simulation of amplitude statistics.....	33
6.4.3 Simulation of Doppler spectra.....	33
7. TARGET DETECTION.....	35
7.1 Parametric modelling	36
7.2 Optimal and sub-optimal detection	37
7.3 Polarimetry.....	37

8. CONCLUSIONS.....	39
REFERENCES	40

Figures

Figure 1:	General trends in clutter behaviour above 10 degrees grazing for average wind speeds (15 knots) for 3 to 10 GHz radar frequency.....	3
Figure 2:	Schematic illustration of first order Bragg resonance for radar wavelength λ and ocean wavelength Λ	5
Figure 3:	Variation of σ^0 with wind speed and grazing angle, X-band, VV pol.	11
Figure 4:	Variation of σ^0 with wind speed and grazing angle, X-band, HH pol.	11
Figure 5:	Circular spotlight mode collection for the Ingara data.	14
Figure 6:	Variation of σ^0 with wind at various incidence angles at 10 GHz, looking upwind.....	18
Figure 7:	Variation of σ^0 with azimuth angle at various frequencies.....	19
Figure 8:	σ_u^0 as a function of grazing angle, looking upwind, for various wind speeds.	19
Figure 9:	IRSG-LIN example azimuth with wind speed $U=10.3$ m/s.	21
Figure 10:	K distribution shape parameter, ν , as a function of azimuth angle (20° graz. angle)... ..	22
Figure 11:	K distribution shape parameter, ν , as a function of azimuth angle (40° graz. angle)... ..	23
Figure 12:	Upwind comparison plots - false alarm rate (\log_{10}) and the relative threshold error between the K-fit and data.	24
Figure 13:	Variation of ν with grazing angle from Ingara	25
Figure 14:	Variation of the KK parameters from an example day of Ingara data.	26
Figure 15:	Range (spatial) correlation.....	32
Figure 16:	Azimuthal (temporal) correlation	32
Figure 17:	Doppler spectra comparison.	34
Figure 18:	Target detection regions.....	35
Figure 19:	P_d variation with polarisation.....	36
Figure 20:	The Cloude-Pottier entropy-alpha angle scatter plots.....	38
Figure 21:	Variation with respect to polarisation and azimuth angle of the target to clutter ratio at 40° grazing.....	39

Tables

Table 1:	Douglas sea state table with metric units. It is assumed the wind speed is measured at 10 meters above the sea surface.....	8
Table 2:	Mean backscatter at 10° grazing angle.	9
Table 3:	Mean backscatter at 30° grazing angle.	10
Table 4:	Mean backscatter at 60° grazing angle.	10
Table 5:	Upwind/downwind and upwind/crosswind ratios.....	12
Table 6:	Wind and wave ground truth for the Ingara data.	14
Table 7:	Ingara radar and trials parameters.....	14
Table 8:	Parameters $G(\theta)$ and $H(\theta)$ for Ulaby model.	17
Table 9:	Parameters $G(\theta)$ and $H(\theta)$ for Masuko model	18
Table 10:	Masuko model coefficients.....	18
Table 11:	IRSG-LIN model coefficients.....	21
Table 12:	IRSG-HYP model coefficients.	21

UNCLASSIFIED

DSTO-GD-0736

This page is intentionally blank

UNCLASSIFIED

1. Introduction

The purpose of this report is to assist with the analysis of high grazing angle sea-clutter being performed by members of the SET-185 panel. This panel is working to address the question: 'can we detect small targets from higher grazing angles?' and 'what are the performance trade-offs?'

This report reviews the published literature on the characteristics of mono-static radar sea-clutter observed with high grazing angles, typically defined to be above 10° . Much of the analysis and modelling of sea-clutter has been undertaken at low grazing angles with the main application being for surface and airborne maritime radars. These typically operate at low grazing angles either from necessity or to achieve the best detection performance against small targets. However, there are growing operational requirements to undertake maritime reconnaissance using radar on high-flying air vehicles, especially UAVs. It has therefore become important to better understand the characteristics of sea-clutter observed at higher grazing angles. For example, a radar at 30,000 feet looking at the sea surface 27 NM away will view the sea at a grazing angle of 10° .

Section 2 of this report covers material related to the specific scattering mechanisms in the plateau region, which is the grazing angle region 10° - 50° . This sets the scene for the subsequent analysis which focusses on the many different aspects of the radar sea-clutter. Much of the literature on high grazing angle sea-clutter measurements dates from 25 years ago, or more, and there are relatively few studies that have been performed recently. Section 3 provides a brief summary of those experiments.

The mean backscatter is the first parameter of interest and is covered in Section 4. One of the key reasons for studying high grazing angle sea-clutter is that the mean backscatter increases linearly with increasing grazing angle. While not necessary a key parameter which effects target detection, many amplitude distributions use the mean to describe the spread of the distribution. If the mean increases, then the spread may broaden and target detection will become a more difficult problem at higher grazing angles.

The next parameter of interest is the amplitude distribution of the radar sea-clutter, as it is used extensively in target detection schemes. Section 5 looks at the amplitude distributions which have been used to model radar sea-clutter from high grazing angles.

Section 6 covers the spatial and temporal correlation of high grazing angle sea-clutter which is directly linked to the Doppler spectrum via a Fourier transform. If the radar sea-clutter is correlated, then target detection schemes must take that into account or they may not perform as expected. A method for simulating coherent sea-clutter is also presented in this section.

Section 7 is the last review section and looks at the research being performed in parametric, optimal, sub-optimal and polarimetric detection schemes at high grazing angles. Parametric modelling is used to describe the mean performance of a detection scheme, while the optimal and sub-optimal schemes are focussed on how a real-world radar might detect targets given assumptions about the sea-clutter characteristics. A lot of the work in this section is closely related to the previous section.

2. Background

The radar cross section (RCS) of the ocean is a measure of the backscattered (i.e. reflected) power received from the ocean surface by a radar. The RCS of the ocean depends on the size of the patch of ocean which has been illuminated - the bigger the patch, the larger the measured backscatter. In order to allow better comparisons between different radar systems and imaging geometries, this dependence is usually removed through the introduction of the normalised RCS, σ^0 . This is also referred to as the mean backscatter and is defined as the RCS per unit area of sea surface illuminated. It is a dimensionless quantity and is typically reported in decibels (dB).

The exact nature of ocean backscatter depends on the grazing angle of the incoming radiation as well as the ocean surface roughness and atmospheric effects such as ducting [1]. The latter is often captured by expressing the normalised RCS as $\sigma^0 F^4$, where F is the propagation factor. While this effect can significantly alter the RCS at low grazing angles, it is expected to be less significant as the grazing angle increases.

The grazing angle is defined as the angle between the ocean surface and the incoming radiation. In measuring grazing angles, it is usual to ignore the local variation in the ocean surface slope and use the mean ocean surface level. Alternatively, incidence angle can be used, where the incidence angle is defined to be the angle between the normal to the ocean surface and the incoming radiation.

The general trends for values of the mean backscatter are illustrated in Figure 1. This shows typical results for σ^0 at X-band, for a wind speed of about 15 kts. It can be seen that the mean backscatter which is horizontally transmitted, horizontally received (HH) is generally lower than that for the vertically transmitted, vertically received (VV) over a range of grazing angles from about 10° to 50°. This is called the 'plateau' scattering region. Also shown in Figure 1 is the cross-polarised, VH or HV mean backscatter which is significantly lower than either of the VV or HH values and also does not show much variation with grazing angle over the plateau region.

This section describes the nature and properties of radar backscatter from the ocean surface at higher grazing angles. One of the dominant backscatter mechanisms in the plateau region is Bragg resonance which is first discussed in Section 2.1. However, this model does not explain all of the observed scattering and hence the composite surface model, described in Section 2.2 was introduced. Further experiments then revealed more non-Bragg scattering, which could not be explained. Section 2.3 describes the non-Bragg scattering, also referred to as sea-spikes, which have become very important in recent years as they can be mistaken for targets. The section concludes in Section 2.4 with a review of parameters used to quantify ocean surface conditions. A lot of the content from this section comes from two internal DSTO reports [2, 3].

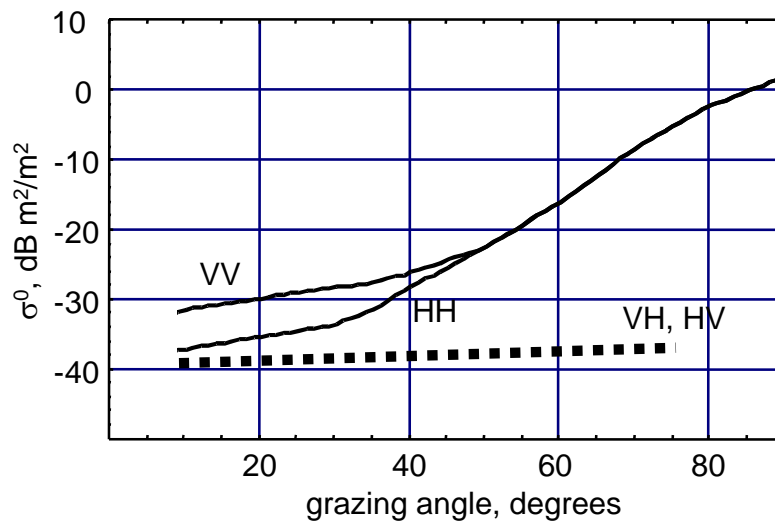


Figure 1: General trends in clutter behaviour above 10 degrees grazing for average wind speeds (15 knots) for 3 to 10 GHz radar frequency.

2.1 Bragg Resonance Scattering Model

Sea water has a high dielectric constant and hence absorbs very little radar energy – most incident radiation is scattered back into the atmosphere. Moreover, there is very little penetration of the ocean surface and so the distribution of scattered energy depends only on the properties of the ocean surface itself. In calm conditions, the ocean surface is flat and radar reflections are highly specular. In this case, most of the transmitted energy is scattered away from the radar and the measured backscatter levels are low. However, as winds increase and the ocean surface becomes rougher, the backscatter pattern becomes more diffuse and measured backscatter levels increase. The qualitative degree of roughness depends on the radar wavelength - the same ocean surface may generate specular reflections at HF frequencies but diffuse reflections at microwave frequencies.

The perturbation theory for electromagnetic scattering was first developed by Rice [4] and later applied by Peake [5] to compute radar cross section. Wright [6] then extended this theory to water and classified it as a 'slightly rough' surface. He showed that the scattering elements of primary importance for grazing angles much less than 90° are capillary or short-gravity waves which satisfy the Bragg equation for a given wavelength and direction of the incidence field.

An early study by Wright [7] suggested that the radar backscatter can be interpreted in terms of wind and wave components. Wright found that the first order Bragg scattering condition can be used to explain data from small amplitude, mechanically generated water waves where the radar backscatter is proportional to the square of the water wave amplitude. However, this first order approximation is only valid when the fetch and wind speeds are very small and consequently, when the backscatter return from the waves are small in amplitude.

A schematic diagram of Bragg resonance is shown in Figure 2. In this figure, the resonant component of the ocean surface spectrum is shown with a bold line and rays depicting the incoming radar waves are shown with lighter lines. First order resonance occurs when the excess distance travelled by the radar waves to successive ocean wave crests are half the radar wavelength λ . In this case, the successive reflections add together in-phase and reinforce or resonate to produce much stronger backscatter than would otherwise be expected. Clearly, this effect also occurs when the excess distance travelled by the radar waves to successive ocean wave crests is any integer multiple of $\lambda/2$. If the grazing angle is denoted by θ and the wavelength of the resonant ocean surface waves by Λ , then the condition for Bragg resonance is

$$n\lambda = 2\Lambda \cos \theta, \quad n = 0, 1, 2, \dots \quad (1)$$

A theoretical backscatter model based on Bragg resonance is presented in Ulaby et al. [8]. They note however, that since their model uses only first order theory, the magnitude of the cross-pol channels HV is predicted to be 0! This is clearly not realistic since in most measured sea-clutter it is non-zero (albeit very low).

Moreover, Wetzel [9], states that “fundamental conceptual problems in applying the Bragg hypothesis in microwave scattering, along with recent questions about the validity of its predictions and the possibility of alternative scattering hypotheses, have reopened enquiry into the physical origins of sea scatter and how best to model it.” Also, the normalised roughness spectrum assumes a linear model for the ocean surface and contains no information on the phase of waves. This means that non-linear effects such as hydrodynamic modulation, whereby the strength and wave number of capillary waves are modified by their location on the large scale waves, are not captured by this model. It is also well known that physical structures with non-Bragg scattering mechanisms are present on the ocean surface, such as breaking waves/white caps, facets generating sea spikes, and foam and spray.

While the Bragg theory above does not match measured backscatter data well, it does provide some insight into properties of measured backscatter data. For instance, it is known that backscatter measured with a VV polarisation channel is larger than that measured with an HH polarisation. Bragg theory explains both this difference due to Fresnel reflection coefficients [8] and also the sinusoidal-like variation in ocean backscatter with azimuth angle. This variation is due to a corresponding variation in the directional spreading function associated with the normalised roughness spectrum. The directional spreading function is commonly modelled with functions of the form $\cos(2\phi)$ which clearly have a sinusoidal-like variation.

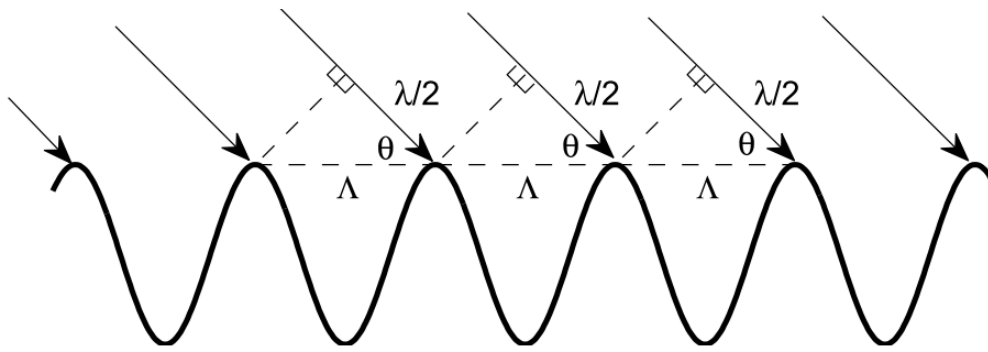


Figure 2: Schematic illustration of first order Bragg resonance for radar wavelength λ and ocean wavelength Λ . The scattered waves add in phase and hence reinforce each other (reproduced from [2]).

2.2 Composite Surface Model

To extend the first order Bragg scattering theory, two scale composite surface theories were proposed to divide the rough surface into large and small-scale components. The large scale component is treated by geometric or physical optics and the small-scale component by the existing perturbation theory. A number of authors have looked at variations of this theory [7, 10-13].

A different approach to explain the radar backscatter was adopted by Valenzuela & Laing [14] who used hydrodynamic models to justify the two-scale composite model. This provides a more physical description of the sea surface where large swells are present with short gravity and capillary waves superimposed. Effects of the sea and swell are included by considering changes in scattering caused by the 'tilting' of the short gravity and capillary waves by the sea and swell. Studies using this theory focused on the spectral width and location of the Doppler shift [14-16]. Hicks et al. [15] studied data at X-band with low grazing angles and found for some experimental conditions that the Doppler bandwidth was proportional to the wind speed and also to the ratio of the significant wave height and wave period. Bass et al. [12] later gave a theoretical basis for the width of the Doppler spectrum being proportional to the ratio of wave height to wave period.

Experimental data with higher wind speeds then started to reveal more than one significant component to the Doppler spectrum. For low sea-states, Hicks et al. [15] found that the spectrum had a Gaussian shape which broadened as the wind speed increased and became asymmetrical. Similarly, for high sea-states, an extra spectral component due to sea-spray was observed by Money et al. [17]. Wright [7] and later Duncan et al. [18] also found a second component which could not easily be explained using the composite scattering theory. This was found at low grazing angles, particularly with the horizontal polarisation. Other authors [14, 16, 19] found the Doppler spectra shifted to a much higher level for the HH channel than the VV channel, which is contrary to the composite surface theory and states that the Doppler shifts should be identical, aside from a small difference due to power-frequency correlations as noted by Hasselmann & Schieler [13]. Also, the above

theory implies that the instantaneous polarisation ratio (HH/VV) should be bounded by an upper limit of 0 dB, which was found to not always hold, [20].

Nevertheless, a number of authors have used or extended the composite surface model to account for these changes. Duncan et al. [18] used a wave tank to vary the fetch and proposed that at lower grazing angles, there are both free and bound capillary waves. At high wind speeds, the bound waves are then tilted by the dominant wave and travel at the same speed. The authors of [21, 22] propose that 'wedge scattering' is present at low grazing angles where surface elements are present with a small radius of curvature relative to the radar wavelength. This mechanism is meant to explain the larger backscatter return when large scale waves are near breaking. Lyzenga et al. [23] then showed how to combine the wedge scattering theory with the composite surface model. Plant [24] proposes that in the low grazing region, wind causes intermediate waves to travel on the underlying swell which are steep enough that some of the short capillary waves are bound to it. Hence, they travel at a faster speed causing a larger Doppler shift.

2.3 Sea-Spikes

Over the past years, a number of authors have proposed different theories to explain the sea dynamics due to non-Bragg scattering, [18, 20, 25-29]. These are primarily concerned with analysis of breaking waves and understanding the main components of the associated radar response. Non-Bragg scattering is commonly represented as a single component and referred to as 'sea-spikes'. A common definition of a sea-spike is a radar return which has a large Doppler component with a wide bandwidth, strong backscatter power as well as a HH return that is equal to or greater than the VV return. Lee et al. [20] summarises three possibilities to explain the phenomena which contribute to non-Bragg scattering:

- There is a wave which is about to break and has a much longer wavelength than the Bragg resonant wave.
- There is a breaking wave which has a long wavelength and large specular return.
- There is attenuation in the VV channel due to Brewster angle damping and the HH channel is affected by multipath scattering and shadowing of the wave troughs by large crests.

Alternatively, Long [30] has distinguished sea-spikes by their duration, with some lasting for a short time before fading rapidly and others persisting for 1-2 seconds. The second type are what are commonly mistaken for targets as they may exhibit many of the same characteristics including polarisation independence.

For the third point, the Brewster angle is the point at which the incident signal completely passes through the sea-surface with no reflection and depends on the ratio of the refractive indices of the two media. This has been calculated to be approximately 7° grazing at X-band, [31] and its effects observed in data collected as high as 20° [32]. The effect of Brewster angle damping is that more of the incident signal will penetrate the water from vertically polarised signals than from horizontal ones, [16]. The result for the backscattered signal (in the power

domain) is a polarisation ratio of 12 dB or greater. More information on Brewster angle damping can be found in [16, 32, 33].

2.4 Wind speed, wave height and sea state

Ocean waves can be divided into two types depending on which physical force governs the wave motion: capillary waves or gravity waves. For capillary waves, the dominant restoring force is surface tension, while for gravity waves, it is the gravitational force. Capillary waves are small and have wavelengths of only a few centimetres or less [30], while gravity waves can be much larger.

The main driving force generating the wave structure on the ocean surface is the wind. Wind energy is transferred to the ocean surface through the surface stress, which varies roughly as the square of the wind speed [34]. The formation of capillary waves is very sensitive to the wind and generally their size reflects the instantaneous strength of the local wind. If the wind stops, the capillary waves soon flatten and disappear [30]. When using wind speed as a parameter, care must be taken to specify the height above the ocean surface at which it is measured, since wind speed varies with height. The exact nature of this variation is complicated and involves the difference in temperature between the ocean surface and the surrounding air layer, amongst other things.

Gravity waves on the other hand persist and large gravity waves can travel long distances. Wind energy is also imparted directly into the gravity waves. Tucker and Pitt [35] note that the process can be thought of as the formation of an eddy on the downwind side of the wave which creates a pressure difference across the wave. Once wind energy has entered the wave system, it is transferred from one part of the spectrum to another via (weak) non-linear interactions [35]. A further complexity of the wave structure is that large gravity waves can propagate large distances. Thus the wave spectrum of interest can contain wave energy imparted from outside the local area. In fact, the large scale wave structure of the ocean surface can often be divided into two components: the sea and the swell [30]. The sea is composed of relatively steep, short-crested waves produced and driven by the wind. These waves are also known as wind waves and travel more or less in the same direction as the wind. The swell, on the other hand, consists of waves which have propagated into the region of interest from distant storms and therefore do not necessarily travel in the same direction as the wind. Swell waves tend to be low frequency (large wavelength) and very sinusoidal-like [30]. Nathanson [36], quotes periods of 6 to 16 seconds as typical of swell.

For the large scale roughness, two different measures are commonly used in maritime applications: sea state and significant wave height. The term sea state can be ambiguous and should be used with care [37]. In fact, it is generally not used at all in the science of oceanography. It originated during the sailing era and was based on visual estimates of the ocean roughness. It was formally included as one element in a universal system of observations at sea as early as 1853. However, ambiguity in the meaning of sea state has evolved with the meaning depending on whether or not the sea surface is decomposed into separate sea and swell components. This problem is ignored by making the assumption that no swell component is present and that the sea is 'fully developed'. The significant wave

height was proposed as a measure of the wave height by a ‘trained observer’. By definition, it is the average height of the highest one-third of all the waves and is denoted by $H_{1/3}$.

The Douglas sea state table shown Table 1 in is typically used to relate the wind speed and significant wave height to a given sea-state. The table is based on the Pierson-Moskowitz spectrum model and indicates the fetch and duration required to generate a fully developed sea for various wind speeds. In this state, the speed of the largest waves matches the wind speed and no further energy can be imparted into the system. Typically, however, the wind will change strength or direction before this state is reached and seas are not usually fully developed.

Table 1: Douglas sea state table with metric units. It is assumed the wind speed is measured at 10 meters above the sea surface (reproduced from [38]).

Sea state	Description	Wave Height (m)	Wind Speed (m/s)	Fetch (km)	Duration (h)
1	Smooth	0.0–0.3	0.0–3.1	-	-
2	Slight	0.3–0.9	3.1–6.2	93	5
3	Moderate	0.9–1.5	6.2–7.7	222	20
4	Rough	1.5–2.4	7.7–10.3	278	23
5	Very rough	2.4–3.7	10.3–12.9	370	25
6	High	3.7–6.1	12.9–15.4	556	27
7	Very high	6.1–12.2	15.4–25.7	926	30
8	Precipitous	> 12.2	> 25.7	1296	35

3. Measured Data Sets

Sea-clutter studies at high grazing angles have been performed from a number of different platforms and locations including cliff tops, observation platforms, boats, planes and wave tanks. The following section outlines the main data sets which have been reported in the open literature.

The earliest efforts to understand sea-clutter phenomenology date from the 1960s and 1970s and many of the details of these studies are difficult to obtain. However, a summary of much of this work with tables of measured values are given in Nathanson [36], with some reproduced in Section 3.1.

There have also been a large number of wave tank studies, with a few focussing on the high grazing angle region, [18, 39-43]. Using a wave tank allows a much more controlled environment with respect to the wind direction, speed and waves. They are however unable to fully replicate the long scale swells that are present in the ocean.

A number of relevant studies by Guinard and Daley [10], Masuko et al. [44], Jessup et al. [25, 26] and Lee et al. [20] are now presented. These studies each focused on understanding different aspects of sea-clutter phenomenology at high grazing angles. The final data set

described below, which is also the most recent was collected by the Australian DSTO imaging radar system known as Ingara [45-47].

3.1 Nathanson data

The Nathanson data [36] lists backscatter values obtained from about 60 experiments. They cover a range of different grazing angles including 0.1°, 0.3°, 1.0°, 3.0°, 10°, 30° and 60°. The values in the tables are primarily compiled from experimental data but contain some extrapolation and interpolation where it is believed to be in error. Unfortunately, no variation with azimuth angle (relative to the wind direction) is given, and instead, the cited backscatter values are averages over all azimuth angles.

The rows of the tables correspond to sea states from 0 to 5 and the columns correspond to different radar frequencies including an X-band frequency of 9.3 GHz. Entries are given for both HH and VV polarisations. The results from 10°, 30° and 60° are reproduced in Tables 2-4.

Table 2: Mean backscatter at 10° grazing angle (reproduced from [36]).

Sea State	Pol.	Mean backscatter, dB below 1 m ² /m ² , at indicated frequency, GHz						
		UHF 0.5	L 1.25	S 3.0	C 5.6	X 9.3	Ku 17	Ka 35
0	V		45			49	45	44
	H		60			56		
1	V				44	42	40	38
	H		56		53	51		
2	V	35	37	38	39	36	34	33
	H	53	53	51	4	43		
3	V	34	34	34	34	32	32	31
	H	50	48	46	40	37	33	31
4	V		31	31	32	31	29	29
	H	48	45		36	34	31	29
5	V	25	28	28	28	26	26	26
	H	46	43	38		31	29	27

Table 3: Mean backscatter at 30° grazing angle (reproduced from [36]).

Sea State	Pol.	Mean backscatter, dB below 1 m ² /m ² , at indicated frequency, GHz						
		UHF 0.5	L 1.25	S 3.0	C 5.6	X 9.3	Ku 17	Ka 35
0	V		42					
	H		50					
1	V	38	38	40	40	39	38	37
	H		46		48			
2	V	30	31	32	34	32	31	30
	H	42	41	40	42	44		
3	V	28	30	29	28	28	23	23
	H	40	39	38	37	34		
4	V		28	27	25	24	24	22
	H		37	37	35	33		
5	V		24			20	21	20
	H		34			24	22	20

Table 4: Mean backscatter at 60° grazing angle (reproduced from [36]).

Sea State	Pol.	Mean backscatter, dB below 1 m ² /m ² , at indicated frequency, GHz						
		UHF 0.5	L 1.25	S 3.0	C 5.6	X 9.3	Ku 17	Ka 35
0	V	32	33	34	35	36	28	
	H	32	32	32		34		26
1	V	23	22	24	26	28		26
	H	22	24	25	26	26		
2	V	20	21	21	23	20	18	19
	H	22	21		22	23		
3	V	18	18	19	18	17	14	14
	H	21	20		20	21		
4	V	14	15		15	14	11	10
	H		18					
5	V		20			10	6	4
	H		18			12	8	

3.2 NRL 4FR

An extensive set of measurements using the NRL 4FR systems was reported by Guinard and Daley [10], with reflectivity measurements made simultaneously in P, L, C and X-bands over grazing angles from 5° to 90° and wind speeds from 0 to 24 ms⁻¹. Their mean backscatter results are shown in Figures 3-4, which also show theoretical predictions of reflectivity based on scattering from a composite surface.

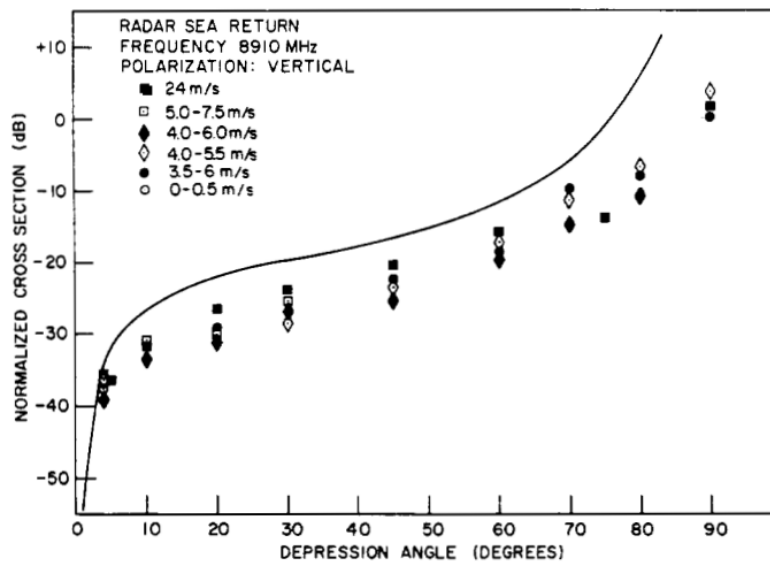


Figure 3: Variation of σ^0 with wind speed and grazing angle, X-band, VV pol; solid line shows composite scattering model prediction (reproduced from [10]).

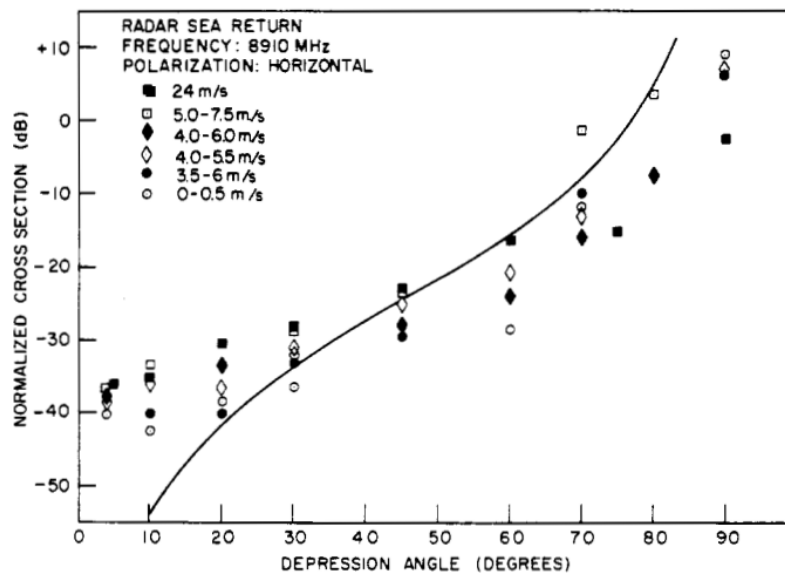


Figure 4: Variation of σ^0 with wind speed and grazing angle, X-band, HH pol; solid line shows composite scattering model prediction (reproduced from [10]).

3.3 Masuko data

A comprehensive set of high grazing angle clutter measurements was published by Masuko et al. [44] in 1986 based on experiments conducted in 1980 and 1981 in two open ocean locations off Japan. They reported measurements of σ^0 in X and Ka-bands with VV and HH polarisations.

Circular flight paths were used to make measurements over all azimuth angles (0° - 360°) for each selected grazing angle and several repeat orbits were flown to obtain statistically representative samples. All flights were conducted at a height of 3100 m. The selected grazing angles were 20° - 90° in 10° increments. Averaging of the repeated backscatter measurements was done in the dB domain and the standard deviation was found to be in the range 0.3 to 1.0 dB.

The ocean surface conditions at the time of data collection were measured using a meteorological buoy at the first location and manually from a boat at the second location. The reported wind speeds: 3.2, 7.9, 9.3 and 14.5 m/s represent average values and were assumed to be uniform over the experimental area. Table 5 taken from [44], shows values of the ratios of the upwind to downwind peak values, σ_u^0/σ_d^0 and of the upwind peak to crosswind minimum, σ_u^0/σ_c^0 , averaged over a range of wind speeds. These ratios all show a minimum reflectivity in the crosswind direction.

Table 5: Upwind/downwind and upwind/crosswind ratios (reproduced from [44]).

	Pol.	Freq (GHz)	Grazing Angle, (deg)					
			20	28	38	48	58	68
σ_u^0/σ_d^0 dB	HH	10	4.16	3.66	2.59	2.24	2.46	-0.35
		34	3.19	3.99	3.00	2.94	2.65	-0.04
	VV	10	1.14	1.44	0.42	1.25	2.01	0.14
		34	2.88	2.79	2.06	1.22	1.67	0.61
σ_u^0/σ_c^0 dB	HH	10	5.05	6.49	4.93	4.92	4.53	2.32
		34	3.69	5.50	5.17	5.95	4.78	3.20
	VV	10	5.54	5.82	5.01	5.25	4.79	2.20
		34	5.86	6.75	6.83	6.12	4.77	2.76

3.4 MIT Chesapeake bay experiments

Another relevant two part study is by Jessup et al. [25, 26] who used a Ku band scatterometer on an observation platform based 26 m above the Chesapeake bay. They studied breaking waves at a grazing angle of 45° with truth data obtained by a co-located video camera. Their studies focussed on firstly detecting the spike events and then assessing their dependence on the wind and wave conditions.

3.5 TRW Scotland experiments

A comprehensive study on X-band scattering was performed by Lee et al. [20] in 1991 off the west coast of Scotland. They looked at the grazing angle range of 10° to 70° using a coherent scatterometer mounted on the bow of a boat. Their study was based on studying the Doppler spectrum and distinguishing between different scattering mechanisms including 'super' events, which we refer to as sea-spikes.

3.6 Ingara data

Ingara is a fully-polarimetric X-band radar system maintained and operated within the Defence Science and Technology Organisation (DSTO) in Australia [48]. The data set comprises two trials on separate occasions and in two distinctly different regions. The first sea-clutter trial 2004 (SCT04), was conducted in the southern ocean approximately 100 km south of Port Lincoln, South Australia [45, 46]. The site chosen was at the edge of the South Australian continental shelf where there was little chance of shallow water affecting the wave field. During the trial, ocean backscatter was collected for a range of different geometries on eight separate days with different ocean conditions. The second maritime surveillance trial 2006 (MAST06), was conducted in littoral and open ocean environments near Darwin in the Northern Territory. Again, data was collected for a range of different geometries and ocean conditions. In this trial, a total of four days data were collected: two of the days were in the littoral zone approximately 25 km north of Darwin and the other two days were in the open ocean approximately 200 km west of Darwin.

During the ocean backscatter collections, Ingara was operated in the circular spotlight-mode as shown in Figure 5. In this mode, the aircraft flies a circular orbit in an anti-clockwise direction (as seen from above) around a nominated point of interest, while the radar beam is continuously directed toward this point. Radar echo data is continuously collected during the full 360° orbit, with the instantaneous PRF appropriately adjusted to maintain a constant spatial separation between pulse transmission positions

Each collection of data in this mode is referred to as a 'run' and there may be several complete orbits in a single run. In order to examine the effect of grazing angle on ocean backscatter, runs were made with different altitude and orbit diameters. For both the SCT04 and MAST06 trials, data was collected at the centre of the spotlight for the nominal grazing angles of 15° to 45° in 5° increments.

Owing to the beamwidth of the radar, its footprint on the ocean surface has a significant range extent. This means that the grazing angle varied across the footprint. It follows that, with appropriate range compression and data processing, the variation in backscatter with grazing angle across the range extent of the radar beam footprint can be measured.

Note that the aircraft speed was approximately 200 knots and so a 1.5 NM orbit took approximately 3 minutes while a 1.9 NM orbit took 3.5 to 4 minutes. The total collection across all grazing angles took approximately 90 minutes. It is reasonable to assume that over such short time intervals, the ocean surface conditions are relatively unchanged and that mean backscatter variations are mostly due to the changing imaging geometry rather than changing ocean conditions.

Nevertheless, it is possible that wind gusts and changes of wind strength and direction may have affected the measurements. Table 6 shows the wind and wave ground truth for the data. The majority of collections on these days used the full-pol mode with a PRF of approximately 300 Hz, with a small number of dual-pol collects with a PRF of close to 600 Hz. Other relevant parameters are summarised in Table 7.

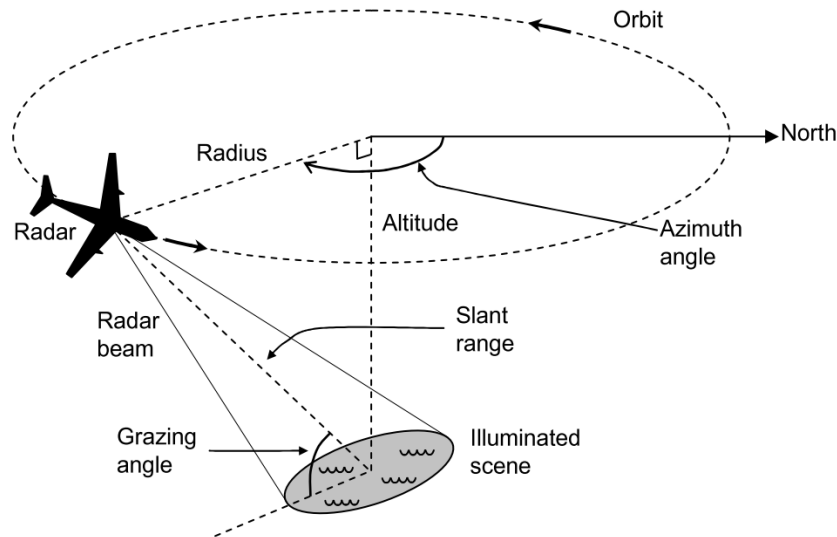


Figure 5: Circular spotlight mode collection for the Ingara data (reproduced from [2]).

Table 6: Wind and wave ground truth for the Ingara data. Directions are 'from' and not 'to'. (reproduced from [2]).

Trial	Flight	Date	Wind		Wave		
			Speed (m/s)	Direction (deg)	Height (m)	Direction (deg)	Period (s)
SCT04	F33	9/8/04	10.2	248	4.9	220	12.3
SCT04	F34	10/8/04	7.9	248	3.5	205	11.8
SCT04	F35	11/8/04	10.3	315	2.6	210	10.4
SCT04	F36	12/8/04	13.6	0	3.2	293	8.8
SCT04	F37	16/8/04	9.3	68	2.5	169	9.7
SCT04	F39	20/8/04	9.5	315	3.0	234	11.4
SCT04	F40	24/8/04	13.2	22	3.8	254	12.2
SCT04	F42	27/8/04	8.5	0	4.3	243	12.5
MAST06	F2	17/5/06	8.5	115	0.62	112	3.1
MAST06	F4	19/5/06	3.6	66	0.25	35	2.6
MAST06	F8	23/5/06	3.5	83	0.41	46	4.0
MAST06	F9	24/5/06	10.2	124	1.21	128	4.6

Table 7: Ingara radar and trials parameters.

Frequency	10.1 GHz
Pulse bandwidth	200 MHz
Pulse length	20 μ s
Polarisations	HH, HV, VV, VH
Grazing Angles	15° to 45°
Range resolution	0.75 m
Cross-range resolution	60 m (typical)

4. Mean Backscatter

There are a number of mean backscatter models in the literature which span regions above 10° grazing. Many of these are based on fitting to Nathanson's tables which were described in Section 3.1. These are summarised briefly in Section 4.1 and include: the NATO AAWSystems model [49], the Naval Environmental Clutter, Attenuation and Propagation Specification or NECAPS model [50], the Technology Services Corporation or TSC model [1] and the NRL model [51].

A second group of mean backscatter models are designed to fit the relationships described by Ulaby et al. [8] for wind speed, grazing and azimuth variations. A description of these relationships are given in Section 4.2 with a summary of the Masuko [44] and Ingara IRSG [52] models which utilise these relationships.

It is observed that for grazing angles less than about 60° that the reflectivity is greater in the upwind direction than in the downwind direction and lowest in the crosswind direction. Some results on the wind direction dependency were reported by Macdonald in [53] at L and X-bands. It is noted that this dependency may be different at lower grazing angles. For example, the Georgia Institute of Technology (GIT) model for reflectivity [54], designed for grazing angles less than 10° , has a minimum reflectivity in the downwind direction.

4.1 Nathanson models

4.1.1 NAAWS model

The NATO AAWSystems or NAAWS model is described in [49] and was designed for shipboard radars which operate at low grazing angles. The model specification draws from a large number of journal publications and standard radar texts. Ducting is not explicitly included, although the model is described as "based on published empirical fits to data that most likely already include some degree of ducting." The model is composed of a reference term and four adjustments parameters for the grazing angle, sea state, polarisation and azimuth angle. The maximum grazing angle that this model is designed for is 30° .

4.1.2 NECAPS model

The Naval Environmental Clutter, Attenuation and Propagation Specification model [50] is described as being a specification "against which weapon system sensors may be designed and their performance evaluated". The specification is intended to provide a set of clutter definitions for the purposes of modelling radar performance and is based on standard radar texts with fits to mean sea-clutter data in Nathanson [36]. The NECAPS model is suitable for predicting mean sea-clutter RCS for grazing angles from 0° to 90° .

4.1.3 TSC model

The Technology Services Corporation or TSC model [1] is a hybrid of two models: (a) for low grazing angles, the model fits curves to the mean sea-clutter data in Nathanson [36] and (b) for high grazing angles, the model is based both on the fitting of data and theoretical considerations as outlined in Beckman [55]. Specifically, the model assumes that two different mechanisms dominate at the different grazing angles: quasi-specular reflection at large grazing angles and diffuse scattering at low grazing angles. The total backscatter is then the sum of these two components, making this model also suitable over the grazing angle range 0° to 90° . The model was later modified in [56] to correct a predicted minimum in the downwind direction that was inconsistent with observations. This change resulted in the model predicting a minimum in the crosswind direction consistent with measurements.

4.1.4 NRL model

A model recently published from NRL [51] is a further attempt to produce a model that fits to the Nathanson data. This model minimises the deviation between predicted and experimental results and can be applied at grazing angles from 0.1° to 60° and radar frequencies from 0.5 GHz to 35 GHz.

4.2 Ulaby Models

An approach to modelling the mean backscatter at grazing angles above 30° is described by Ulaby et al. [8]. The variation of σ^0 with grazing angle, θ , is modelled for each of the upwind, σ_u^0 , downwind, σ_d^0 , and crosswind, σ_c^0 , directions using a relationships of the form:

$$\sigma_u^0(\theta)_{dB} = G_u(\theta) + H_u(\theta) \log_{10} U, \text{ dB} \quad (2)$$

where U is the wind speed in ms^{-1} . This relationship is quite accurate for the plateau scattering region. Equation (2) shows the relationship for the upwind direction and similar relationships are defined for the downwind and crosswind directions. The variation with azimuth look direction, ϕ , is then modelled using

$$\sigma^0 = a_0 + a_1 \cos \phi + a_2 \cos(2\phi), \quad \text{m}^2/\text{m}^2 \quad (3)$$

where,

$$\begin{aligned} a_0 &= \frac{\sigma_u^0 + 2\sigma_c^0 + \sigma_d^0}{4}, \\ a_1 &= \frac{\sigma_u^0 - \sigma_d^0}{2}, \\ a_2 &= \frac{\sigma_u^0 - 2\sigma_c^0 + \sigma_d^0}{4}. \end{aligned} \quad (4)$$

Values for $G(\theta)$ and $H(\theta)$ for some values of θ and for VV and HH polarizations at 14.65 GHz are given by Ulaby et al. [8] and reproduced in Table 8.

Table 8: Parameters $G(\theta)$ and $H(\theta)$ for Ulaby model (reproduced from [8]).

Pol.	Wind		Grazing Angle, θ (deg)			
			40	50	60	70
HH	Upwind	G	-33.87	-30.56	-23.67	-10.51
		H	9.90	15.40	17.10	17.20
	Downwind	G	-40.51	-35.53	-25.69	-10.97
		H	22.40	21.10	17.20	10.60
	Crosswind	G	-48.86	-42.92	-31.87	-13.57
		H	25.80	23.60	18.80	10.10
VV	Upwind	G	-44.81	-35.85	-24.23	-10.16
		H	22.40	19.10	14.80	9.60
	Downwind	G	-48.24	-39.21	-27.12	-11.88
		H	23.90	20.80	16.30	10.40
	Crosswind	G	-54.20	-44.69	-31.43	-13.41
		H	26.60	22.90	17.60	9.90

4.2.1 Masuko model

In their analysis of the data, Masuko et al. [44] did not develop a complete model of σ^0 involving all the independent variables together, rather the dependencies were modelled in isolation from one another. Five different variables were considered: radar frequency, polarisation, wind speed, grazing and azimuth angles.

Masuko used the same modelling approach as Ulaby et al. [8] for the grazing and azimuth variations with Table 9 showing their results at X-band. Some typical results showing variation in wind speed and azimuth angle are presented in Figures 6-7. Note that these figures use incidence rather than grazing angle.

They then extended these results by interpolating for intermediate values of grazing angle to use in Equation (2) and then modelled the variation with look direction using Equations (3) and (4). As an example, the values of G and H in Table 9 have been fitted to a quadratic dependence on θ of the form:

$$\begin{aligned} H &= h_1 + h_2\theta + h_3\theta^2 \\ G &= g_1 + g_2\theta + g_3\theta^2 \end{aligned} \quad (5)$$

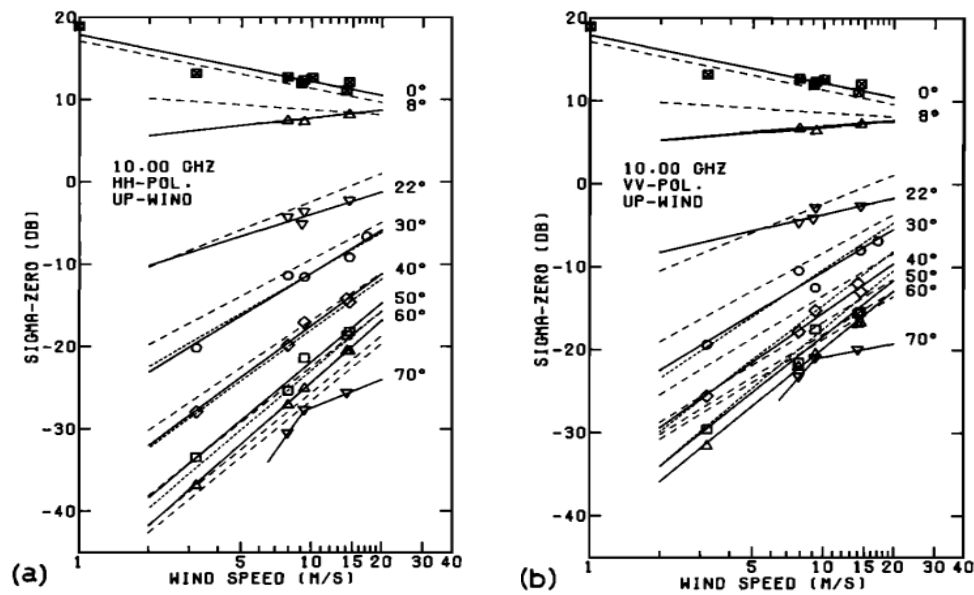
where θ is the grazing angle in degrees. Table 10 shows the values of the parameters achieved, with a validity of $30^\circ \leq \theta \leq 60^\circ$. Using these parameters, Table 8 shows an example of the variation of σ_u^0 with grazing angle, looking upwind, for VV and HH polarizations.

Table 9: Parameters $G(\theta)$ and $H(\theta)$ for Masuko model (reproduced from [44]).

Pol.	Direction		Grazing Angle, θ , (deg)			
			30	40	50	60
HH	Upwind	G	-49.25	-45.47	-38.26	-28.27
		H	24.92	23.63	20.83	17.2
	Downwind	G	-54.04	-51.78	-42.71	-29.96
		H	26.96	28.23	23.04	16.92
	Crosswind	G	-56.36	-50.27	-41.52	-31.34
		H	26.34	23.7	18.61	16.28
VV	Upwind	G	-42.81	-40.77	-35.34	-27.62
		H	22.96	22.4	19.77	17.04
	Downwind	G	-43.64	-43.27	-38.07	-30.08
		H	23.09	24.88	21.04	17.87
	Crosswind	G	-45.99	-44.64	-38.07	-30.74
		N	20.48	21.2	16.9	15.48

Table 10: Masuko model coefficients from Table 9 fitted to Equation (5).

Pol.	Wind	Coefficients ($30 \leq \theta \leq 60$ degrees)					
		g_1	g_2	g_3	h_1	h_2	h_3
HH	Upwind	-42.38	-0.69	0.015	22.21	0.26	-0.006
	Downwind	-31.38	-1.55	0.026	4.57	1.31	-0.018
	Crosswind	-63.16	-0.08	0.010	38.58	-0.42	0.001
VV	Upwind	-32.60	-0.77	0.014	19.41	0.28	-0.005
	Downwind	-23.22	-1.256	0.019	6.93	0.92	-0.012
	Crosswind	-35.00	-0.822	0.015	17.03	0.29	-0.005

Figure 6: Variation of σ^0 with wind at various incidence angles at 10 GHz, looking upwind, for: (a) HH and (b) VV polarisations (reproduced from [44]).

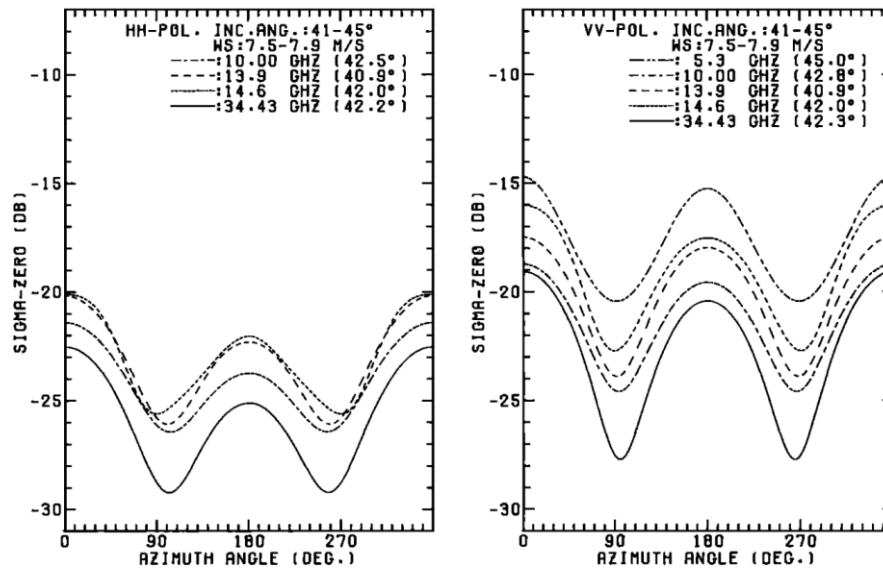


Figure 7: Variation of σ^0 with azimuth angle at various frequencies for HH (left) and VV (right) polarisations (reproduced from [44]).

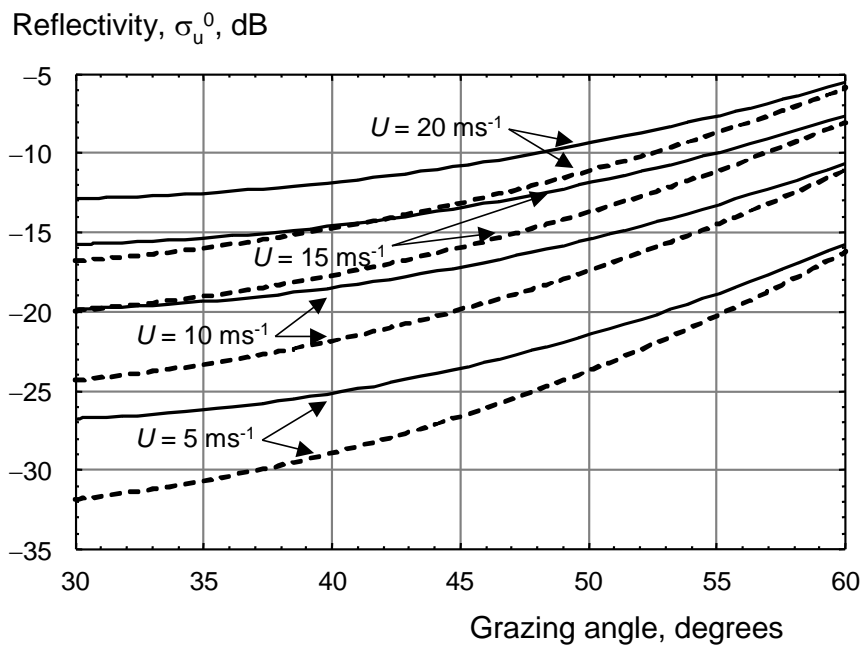


Figure 8: σ_u^0 as a function of grazing angle, looking upwind, for various wind speeds, U : (solid lines) VV pol, (dashed lines) HH pol.

4.2.2 DSTO IRSG models

The DSTO Imaging Radar Systems Group (IRSG) models [52] are based on fitting a large amount of data covering 360° in azimuth and from 20° - 45° in grazing. There were 12 days with slightly different wind speeds. Only absolute values of reflectivity are reported in this reference, but the same trends are observed for σ_u^0/σ_d^0 and σ_u^0/σ_c^0 as earlier results.

The model uses the same relationships as Ulaby et al. [8] for the wind speed, azimuth and grazing angles. Then it goes one step further and combines them together into a single model. It follows from Equation (4), that the full dependence of σ^0 on wind speed and imaging geometry in Equation (3) can be captured by modelling the dependence of σ_u^0, σ_d^0 and σ_c^0 on grazing angle and wind speed alone. This is done by using a two-dimensional polynomial to combine the relations in Equations (2) and (5). The simplest combination uses only the first two components of Equation (5) to form a planar model:

$$\sigma^0(\theta, U)_{dB} = b_0 + b_1\theta + b_2 \log_{10}(U), \text{ dB} \quad (6)$$

The IRSG-LIN model involves fitting this model to backscatter data from each of the three cardinal wind directions: upwind, downwind and crosswind to produce three sets of coefficients (b_0, b_1, b_2). The backscatter coefficients σ_u^0, σ_d^0 and σ_c^0 are then combined using Equation (4) to produce the coefficients (a_0, a_1, a_2) of the model in Equation (3).

A second variation of this model is known as the IRSG-HYP, which is a slightly more complex model and allows for a correlation between the dependence on θ and $\log_{10}(U)$. With this model, the following equation is used in place of Equation (6),

$$\sigma^0(\theta, U)_{dB} = b_0 + b_1\theta + b_2 \log_{10}(U) + b_3\theta \log_{10}(U), \text{ dB} \quad (7)$$

The model coefficients for both of these models are given in Tables 11-12. Figure 9 then shows an example of the IRSG-LIN model compared against F35, which has a wind speed of 10.3 m/s. The upwind direction has been placed in the centre at 0° and bad or missing data is shown by striped diagonal lines.

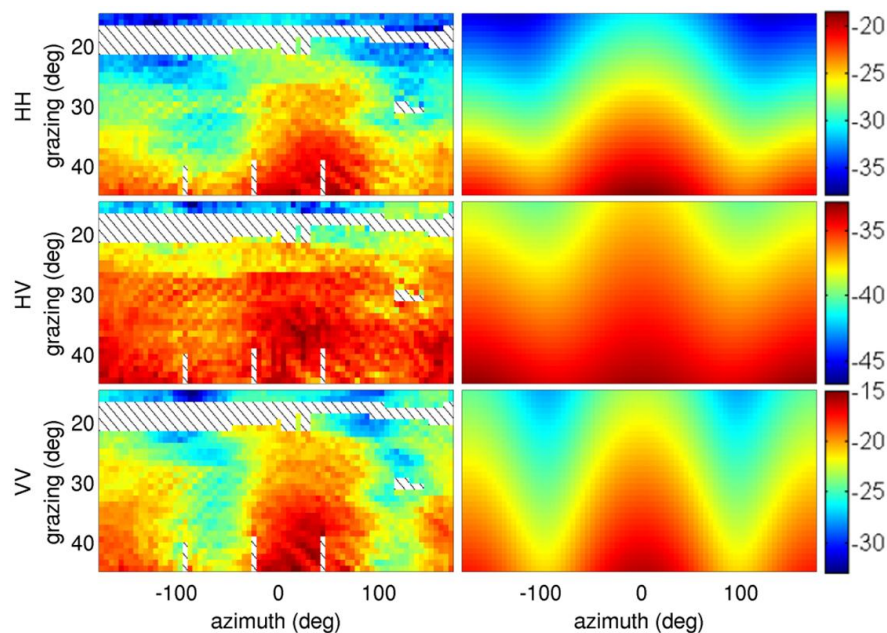
In the paper by Crisp et al. [52], all of the Nathanson based models from this section except the new NRL model, the Masuko model and the GIT model [54], were compared against the Ingara data set. Not surprisingly, the lower grazing angle GIT and NAAWS models did not model backscatter behaviour in the plateau region well. The TSC model showed a consistent trend of under-estimating the Ingara data in the plateau region, especially at the higher grazing angles and low wind speeds. The Masuko models were a reasonably close match to the Ingara data, particularly for VV polarisation. The main discrepancies occur for HH polarisation and especially at low and high wind speeds. As expected, the fit of the IRSG models to the Ingara data was significantly better almost everywhere than any of the other models. The performance of IRSG-LIN and IRSG-HYP are very similar with the only significant difference being at very high grazing angles.

Table 11: IRSG-LIN model coefficients.

Polarisation	Azimuth	Coefficient		
		b_0	b_1	b_2
HH	Upwind	-60.03	23.39	22.65
	Downwind	-67.80	28.58	23.92
	Crosswind	-67.09	23.12	24.71
HV	Upwind	-66.65	9.72	25.46
	Downwind	-68.74	14.17	24.47
	Crosswind	-73.09	14.85	26.66
VV	Upwind	-50.18	12.41	25.15
	Downwind	-50.16	12.30	23.92
	Crosswind	-52.60	12.30	22.09

Table 12: IRSG-HYP model coefficients.

Polarisation	Azimuth	Coefficient			
		b_0	b_1	b_2	b_3
HH	Upwind	-61.78	26.34	24.53	-3.19
	Downwind	-74.47	39.90	31.10	-12.22
	Crosswind	-80.77	46.18	39.37	-24.81
HV	Upwind	-60.99	0.00	19.32	10.57
	Downwind	-69.18	14.94	24.95	-0.83
	Crosswind	-73.86	16.17	27.49	-1.44
VV	Upwind	-40.11	-4.88	14.24	18.80
	Downwind	-37.92	-8.72	10.65	22.86
	Crosswind	-45.26	-0.31	14.13	13.71

Figure 9: IRSG-LIN example azimuth with wind speed $U=10.3$ m/s (dB). Left – Ingara data, right – IRSG-LIN model.

5. Amplitude Distribution

Most studies of sea-clutter amplitude statistics have been undertaken at low grazing angles where the scattering is often dominated by the effects of shadowing and multipath reflections. In this region, the clutter amplitude statistics may become very long-tailed, with a variety of different scattering mechanisms, such as Bragg, whitecap and specular scattering, contributing to clutter spikes [38]. At higher grazing angles however, the backscatter will predominantly be due to Bragg scattering from rough surfaces with a smaller component due to scattering from whitecaps.

Commonly used PDFs include the Rayleigh, log-normal and Weibull, with the latter two used when longer tails were observed in the radar backscatter [30]. A more useful family of distributions however, combines both the Rayleigh speckle fluctuations and the underlying RCS components into a 'compound' representation. The most widely used is known as the K distribution, which models the underlying RCS with a gamma distribution.

Due to the small amount of available sea-clutter data, there are only a small number of studies which have looked at fitting different distributions to the sea-clutter amplitude or intensity [47, 57-64] and all of these have been looked at for fitting to the Ingara data set described in Section 3.6. The following discussion summarises the different distributions which have been considered over the past years.

The first studies were by Dong and Haywood [47, 61], who reported that whilst the clutter reflectivity varied with look direction, the higher order amplitude statistics were largely independent of look direction. Data was analysed at grazing angles of 20° and 40° and fitted to a K distribution. The estimated shape parameter, ν , as a function of look direction is shown in Figures 10-11 for the two grazing angles. It can be seen that the HH data was usually more spiky (smaller ν) than the VV data, especially at the lower grazing angle.

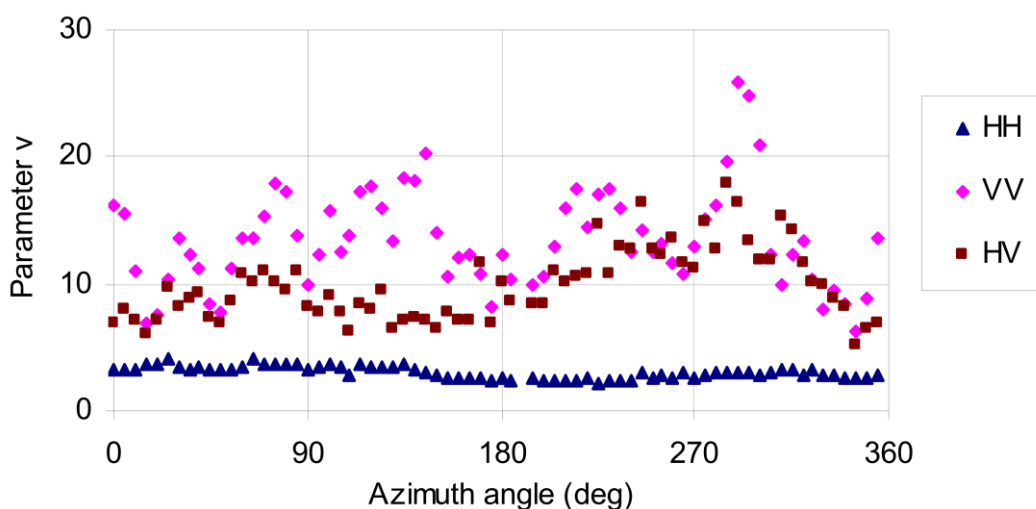


Figure 10: K distribution shape parameter, ν , as a function of azimuth angle (20° grazing angle); upwind direction was about 250° (reproduced from [47]).

Dong also investigated the overall goodness of fit of the data to the K distribution. It was found that the HH data did not usually fit very well in the tails of the distributions, probably due to the presence of discrete clutter spikes. The VV data was consistently a good fit to the K distribution for this data. To better model the fit to the HH data, Dong investigated the use of the KA distribution. The KA distribution fitted the data but was perceived as being too computationally expensive to use in practice.

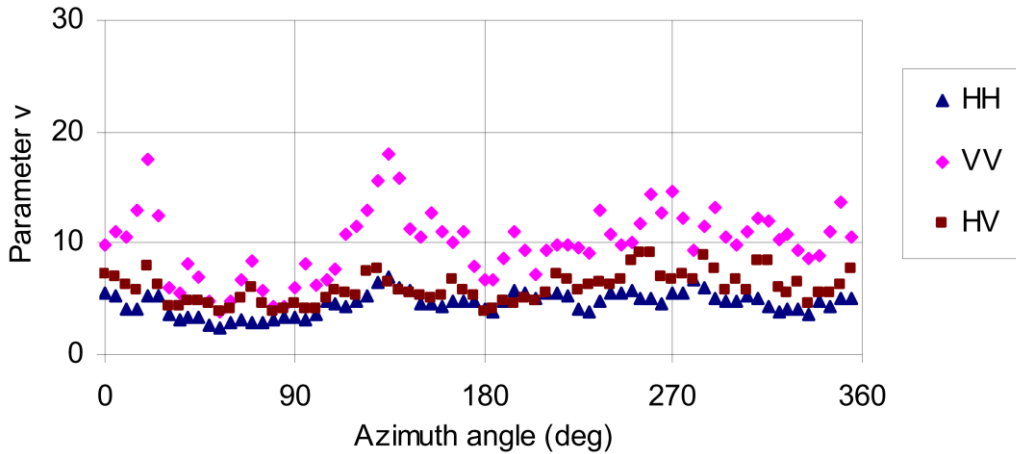


Figure 11: K distribution shape parameter, ν , as a function of azimuth angle (40° grazing angle); upwind direction was about 250° (reproduced from [47]).

Dong therefore introduced the KK distribution to match the data. This model assumes that both the Bragg/whitecap scatterers and the discrete spikes are K distributed (the KA distribution models the spikes as having a Rayleigh amplitude distribution), with the overall PDF, $p(x)$, a mixture of the two K distributions:

$$p(x) = (1-k)p_1(x; \nu, \sigma) + k p_2(x; \nu_{sp}, \sigma_{sp}) \quad (8)$$

where $p_1(x; \nu, \sigma)$ and $p_2(x; \nu_{sp}, \sigma_{sp})$ are K distributions with shape parameter ν and mean intensity σ for the Bragg/whitecap component and ν_{sp} and σ_{sp} for the spike component. The factor k determines the relative contribution of the spikes to the overall clutter return. Dong [47] found that it was satisfactory to set $\nu = \nu_{sp}$, whilst σ_{sp} is defined by a parameter $\rho = \sigma_{sp} / \sigma$. The choice of ρ determines the degree of separation in the tail between the two components, while the value of k determines the level at which they start to diverge. Further analysis of the KK distribution to the Ingara data was reported by Rosenberg et al. [57, 59] where thermal noise and pulse-to-pulse integration were included in the distribution.

Figure 12, taken from [59] illustrates the comparative fits of the K and KK distributions to HH, HV and VV data, with 30° grazing angle, looking upwind. The plots show the error in threshold to achieve a given P_{fa} if the K and KK distributions are used to fit the data. It can be clearly seen that the K distribution is a good fit for the VV polarization data but the KK distribution is needed to fit the HH data and, to a lesser extent, the HV data. Dong [47] also reported the use of a Weibull-Weibull distribution, which was also found to be a good fit to the data.

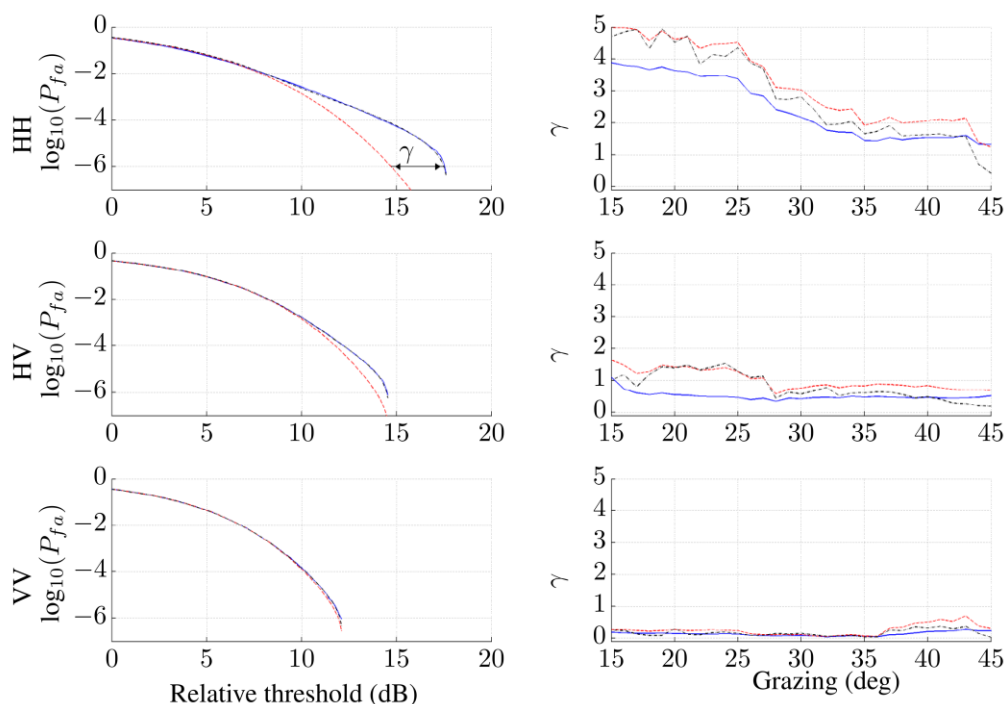


Figure 12: Upwind comparison plots; left: false alarm rate (\log_{10}), 30° grazing: (—) data, (---) K, (- • -) KK; right: relative threshold error between the K-fit and data (dB), $P_{fa} =$ (—) 10^{-4} , (---) 10^{-5} , (- • -) 10^{-6} (reproduced from [59]).

Crisp et al. [60] and Rosenberg et al. [58] undertook further analysis of the Ingara data previously reported by Dong [47] and also data from the MAST06 Ingara trial. This work analysed a much larger data set than [47] and found more evidence of a dependence for the shape on wind direction. The various trends observed for the shape, ν can be summarized as:

- ν increases with grazing angle (i.e. becomes less spiky) for HH and VV data, although the values for VV data were high in all cases and so this trend is weak.
- ν has a generally sinusoidal variation with azimuth, aligned to the wind direction (but not the swell direction), with peaks in the upwind and downwind directions.
- ν increases with coarser range resolution.
- there is a weak tendency for ν to increase with decreasing ocean surface roughness in HH and VV.

The trends with grazing angle and range resolution are, at least qualitatively, the same as have been observed at lower grazing angles. However, the relatively limited range of data available at higher grazing angles possibly means that the other two trends are also present at lower grazing angles. Figure 13 shows an example of the shape as a function of grazing angle for the two separate Ingara trials.

The paper by Rosenberg et al. [58] then followed on from this work and looked at both characterising and forming simple parameter models for the K and KK distribution over a

wide range of grazing and azimuth angles. Figure 14 shows the variation of the KK shape and ratio of means parameter for an example day.

The characteristics of the spikes observed in HH data from the Ingara radar trials have been further investigated by Rosenberg [65]. He observed that the majority of spikes occur at the lower grazing angles with HH data. Interestingly, for the VV and VH data, the spike density is slightly higher in the crosswind directions.

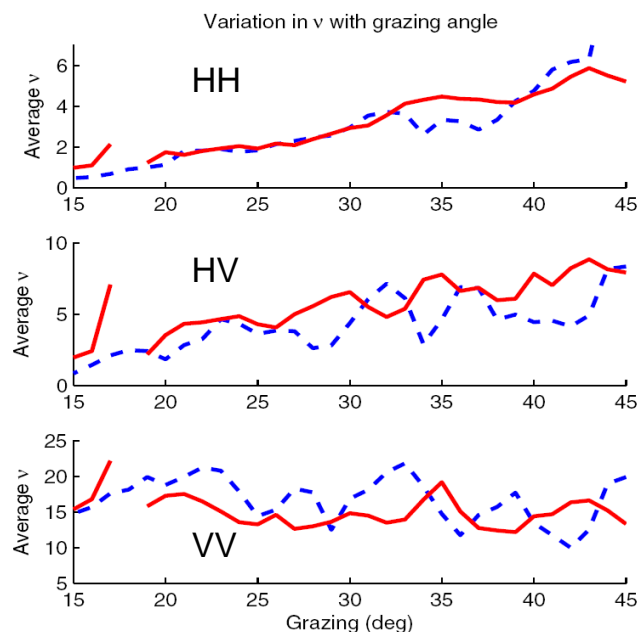
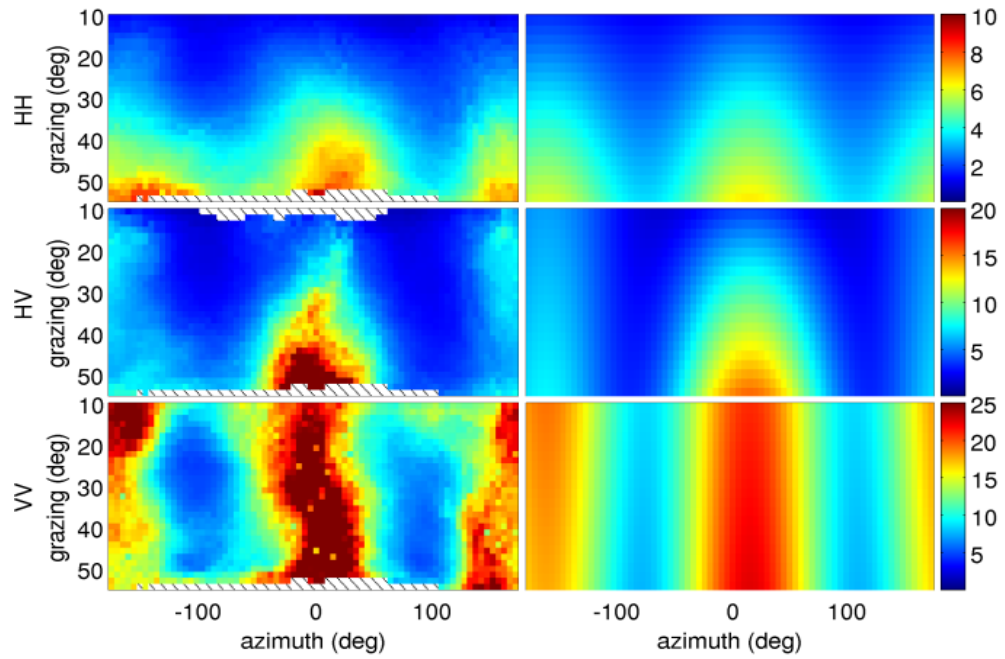
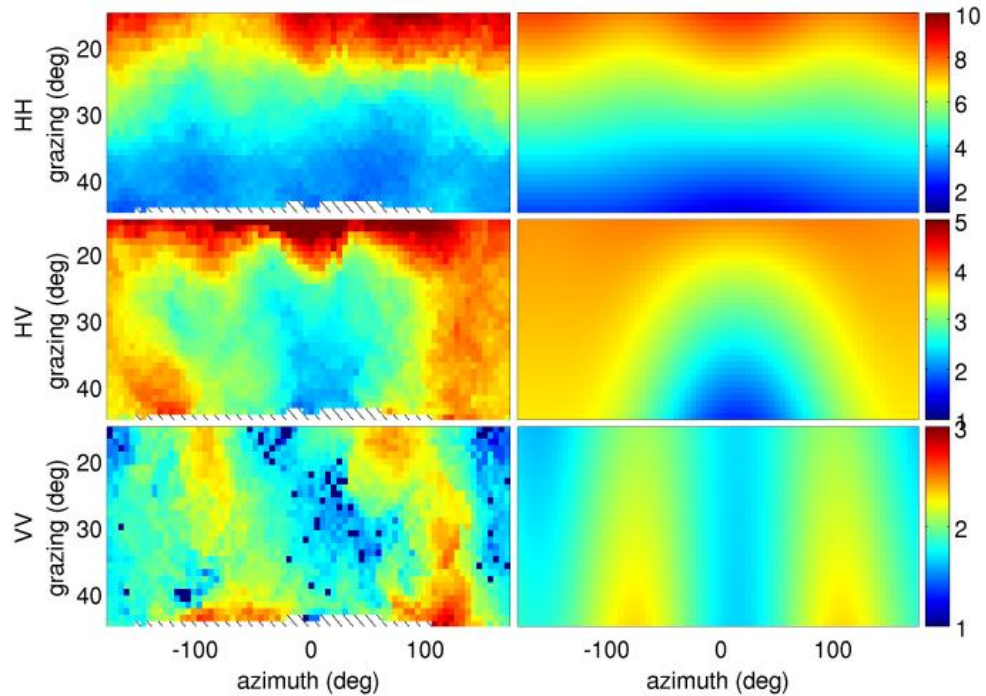


Figure 13: Variation of v with grazing angle from Ingara: (—) SCT04 trial, (---) MAST06 trial (reproduced from [60]).

More recently, Weinberg [62, 63] has investigated the Pareto distribution for fitting to the Ingara data. It was found that this distribution can equally fit the long tails present in the data with the advantage of only requiring two parameters to be estimated. The compound formulation of the distribution is very similar to the K distribution, except that now the underlying RCS is modelled with a negative exponential distribution. A combination Pareto-Pareto distribution [64] was also studied, but found to not offer any significant benefits compared to just a single Pareto distribution. Subsequent work by Rosenberg and Bocquet [66] is now underway to construct a multilook form of this distribution with thermal noise. It is expected that this distribution will offer the best trade-off for complexity with the ability to fit the tail of the distribution with sufficient accuracy. The other key feature of this distribution is that extremely simple optimal and sub-optimal detectors have been formulated. More detail on this is presented in Section 7.



(a) Variation of the KK shape.



(b) Variation of the KK ratio of means.

Figure 14: Variation of the KK parameters from an example day of Ingara data. For each result, the left result is the data, right is the model (reproduced from [58]).

6. Doppler Spectra and Correlation

Knowledge of the mean Doppler spectrum enables the temporal correlation of the sea-clutter to be measured and used for simulation and radar performance analysis. Recent analysis [67] has confirmed that if the temporal correlation is not accounted for correctly, the required signal to interference ratio for a given probability of detection will be incorrect by several dB, resulting in overestimated performance.

There are only a small number of studies which have characterised aspects of the sea-clutter Doppler spectra at high grazing angles and even fewer who have tried to model it. A summary of the main points from the literature which are concerned with the Doppler spectrum is given in Section 6.1. Relevant models are then presented in Section 6.2 for the mean Doppler Spectrum and in Section 6.3 for an analysis of the temporal and spatial correlations. The final Section 6.4 then reports a study by Watts [68] who has modelled the evolution of the Doppler Spectra over time.

6.1 Background

Sea-clutter studies have been performed from a number of different platforms and locations including cliff tops, observation platforms, boats, planes and wave tanks. The majority of studies characterise the Doppler spectrum as a single Gaussian component with an offset and spread. Later studies looked at characterising the spike component of the sea-clutter as it appeared at a higher velocity and altered the Doppler spectrum. Based on the data sets described in Section 3, the following descriptions outline the key points relevant to the Doppler spectrum in the high grazing angle region:

The study by Lee et al. [20] used an X-band coherent scatterometer mounted on the bow of a boat. This enabled them to look at sea-clutter over the grazing angle range of 10° to 70° . They found the following:

- In the upwind direction, as the grazing angle increases, the mean Doppler velocity reduces, approximately in proportion to $\cos(\theta)$ (this was also observed by Nathanson [36]).
- The higher velocity (Doppler) peak observed with HH polarization reduces relative to the peak for VV polarisation, so that at higher grazing angles, typically $\theta > 50^\circ$, the velocities are approximately equal with very similar spectral shapes.
- At upwind as the grazing angle decreases, the HH Doppler peak separates from the VV peak by shifting to a higher frequency.
- At upwind (25° grazing), the non-Bragg spectral peak for the HH polarisation is a few dB larger than the Bragg peak.
- At upwind, by removing the slow-component with a high pass filter, sea-spikes were found at all grazing angles.

- At crosswind, the fast component is much smaller than the slow component and was not observed above 25° grazing. As a result, both the HH and VV spectra appeared the same.
- The decorrelation time determined from the autocorrelation function of the HH and VV spectra increased with grazing angle.

The two part study by Jessup [25, 26] used a Ku band scatterometer on an observation platform based 26 m above the Chesapeake bay. The following observations were made:

- Waves which produced whitecaps were not necessarily associated with a large spike in the radar backscatter. However, many broken waves had an associated spike in the radar backscatter.
- Sea spikes associated with breaking waves tended to be accompanied by an increased mean Doppler frequency and large increases in bandwidth.

There have been a large number of wave tank studies, but only a few have looked at the high grazing angle region, [18, 39-43]. The key points from these studies include:

- The Doppler bandwidth increases with increasing fetch, [18].
- The fast spectral peak becomes stronger as the wind speed increases, [39].
- The non-Bragg returns do not always correspond to wave breaking, [41].
- Rozenberg et al. [42] observed that the effect of long waves/swell can change a significant number of non-Bragg scatterers in the upwind HH backscatter to Bragg scatterers, while for the VV backscatter, the reverse is true at high wind speed and a significant number of Bragg scatterers become non-Bragg. Interestingly, this effect did not appear in the downwind direction.
- Lamont-Smith [43] found that the fast non-Bragg component showed a linear dependence between both the HH and VV Doppler spectral peaks and the grazing angle. This was consistent (albeit with a different slope) over different wind speeds and radar frequencies.

An airborne study of the Doppler spectrum from the NRL 4FR radar [10] was conducted by Valenzuela & Laing [11, 14]. They looked at the polarisation dependence of HH and VV over 10° to 30° grazing and discussed how the azimuth beam pattern will spread the observed scatterer velocities. They claim this effect is minimal and focused their study primarily on the Doppler spectral width, where they found:

- It decreases with increasing radar frequency.
- It is greatest upwind and smallest in the downwind.
- It increases with wave height.
- For the vertical polarisation, it is almost independent of grazing angle, while the horizontal width decreases to the vertical level as the grazing angle increases.

6.2 Mean Doppler spectrum models

There are a few low-grazing angle models which try and capture the experimental spread of the Doppler spectrum. One such model is by Wetzel [9] who modelled the mean velocity of the Doppler spectrum, V_{VV} and V_{HH} when looking upwind or downwind by:

$$\begin{aligned} V_{VV} &= 0.25 + 0.18U \quad (ms^{-1}) \\ V_{HH} &= 0.25 + 0.25U \quad (ms^{-1}) \end{aligned} \tag{9}$$

where U is the wind speed in ms^{-1} . The half-power width, Δ , is quite variable but is given approximately by,

$$\Delta = 0.24U \quad (ms^{-1}) \tag{10}$$

At high grazing angles, Stacy et al. [46] and subsequently Rosenberg et al. [69, 70] have reported analysis of the Doppler spectra observed in the Ingara data. They fitted the observed spectra to the Walker model [31, 71], which describes the long-term average spectrum in terms of three Gaussian components. The average spectra were fitted to the Walker model using a 'best-fit' algorithm, also taking into account the effects of platform motion on the observed spectra. The Walker model identifies three components of the spectrum due to Bragg scattering, whitecap scattering and sea spike (specular) scattering. The analysis in [69] confirmed the bimodal nature of the average Doppler spectrum, with slower Bragg and faster whitecap components comprising the majority of the spectrum. However, it was also found that Bragg scattering components tended to dominate the returns for this data. This resulted in substantially weaker whitecap and sea-spike components relative to the Bragg component than was observed by Walker at lower grazing angles, where the whitecap component can often be significantly greater than the Bragg component in VV and HH polarizations.

The results in [70] showed typical whitecap Doppler shifts up to ± 100 Hz at X-band (dependent on wind direction) relative to the Bragg component. It was also noted that sea-spikes were not only found in the upwind direction but also at a number of different azimuth directions. Also, from this study, the mean decorrelation times over all azimuth directions were 5 ms for HH and 7 ms for VV. For the HH case, the whitecap magnitude was approximately equal to the Bragg component, except for the crosswind directions when it was less. This would account for the shorter correlation time when averaged over all directions. For the VV case, the Bragg component was dominant in all directions.

However, there was a question raised about whether the third spike component is present in the VV channel when the grazing angle is above 20° and Brewster angle damping is not present. To answer this question, a recent paper characterised the Ingara sea-clutter to distinguish between different types of scattering [65]. This study showed that Walker's model is not entirely suitable at high grazing angles and hence a new two component model was recently proposed to capture both the slow 'Bragg' and the fast 'non-Bragg' or 'sea-spike' scattering. The design of the model accounts for the reduced Brewster angle damping above 20° grazing and allows both HH and VV polarisation channels to receive the fast component, albeit with a different magnitude.

The new two component underlying Doppler spectrum model by Rosenberg [72] uses the Gaussian building blocks that both Walker [31] and Lamont-Smith [43] used. A number of observations from the literature influenced the new model:

- Breaking waves are faster than Bragg waves and thus possess high Doppler velocities, [42]
- Sea-spikes are visible at all grazing angles, [20, 65].
- At higher grazing angles, the Doppler spectrum for both HH and VV are similar, i.e. no Brewster angle damping is present, [20, 65].
- Both discrete and persistent non-Bragg scatterers are present in both HH and VV channels, [65].

The model is based on these considerations and also the fact that the majority of the Ingara data, which was used to verify the model, has been collected at a low PRF making estimation of too many parameters difficult. This model differs to Walker's model in that the persistent whitecap and discrete sea-spike components have been combined into a single component which is present in both HH and VV. The two component model is given by,

$$\begin{aligned}\Psi_{HH}(f) &= \Psi_{B_{HH}}(f) + \Psi_{F_{HH}}(f), \\ \Psi_{VV}(f) &= \Psi_{B_{VV}}(f) + \Psi_{F_{VV}}(f).\end{aligned}\tag{11}$$

where the first component for each polarisation represents the slow Bragg component with the same centre frequency, f_s and width, w_s , but each polarisation has a different magnitude, S_{HH} and S_{VV} . The centre frequency is related the Bragg speed by $f_s = 2v_s/\lambda$ and the 3 dB width of the Gaussian is calculated by $w_{3dB} = 2\sqrt{\ln 2}w$.

$$\begin{aligned}\Psi_{S_{HH}}(f) &= S_{HH} \exp\left[-\frac{(f - f_s)^2}{w_s^2}\right], \\ \Psi_{S_{VV}}(f) &= S_{VV} \exp\left[-\frac{(f - f_s)^2}{w_s^2}\right].\end{aligned}\tag{12}$$

The second component represents the fast non-Bragg component associated with both the discrete and persistent sea spikes. It is assumed that the sea-spike return is present in both polarisations with the same centre point, f_f and width, w_f , but different magnitudes F_{HH} and F_{VV} .

$$\begin{aligned}\Psi_{F_{HH}}(f) &= F_{HH} \exp\left[-\frac{(f - f_f)^2}{w_f^2}\right], \\ \Psi_{F_{VV}}(f) &= F_{VV} \exp\left[-\frac{(f - f_f)^2}{w_f^2}\right].\end{aligned}\tag{13}$$

The estimated model magnitude parameters revealed that the VV channel is 5-10 dB greater than the HH channel. A sinusoidal variation was observed for both channels with maxima in the upwind and downwind directions and minima in the cross wind directions. For the fast magnitude, the HH return was always greater than the VV indicating the presence of

dominant fast components in the HH channel. There is also roughly a 5 dB increase in the magnitude for the downwind HH channel. Both model centre points were found to vary sinusoidally around the upwind direction and there was no discernible trend for the width parameters over azimuth. For variations in grazing angle, there was a trend observed with decreasing value as the grazing increased, which was more pronounced for the fast component.

The final contribution in [72] was to introduce a new model for temporal decorrelation as a function of wind speed and wave height. This directly relates to the parametric performance prediction modelling which is described in Section 7.1.

6.3 Non-coherent correlation analysis

By using the traditional measure of correlation [73] between two radar samples, the short and/or long term characteristics of the amplitude or intensity can be measured. Assuming a sample series $x(k), k = 1 \dots N$ is wide sense stationary, the Pearson correlation coefficient $\rho(l)$ between $x(k)$ and $x(k + l)$ is defined as,

$$\rho(k) = \frac{\langle x(k)x^*(k+l) \rangle - \langle |x| \rangle^2}{\langle |x|^2 \rangle - \langle |x| \rangle^2}, k = 0, 1, \dots \quad (14)$$

Dong [74] has studied the azimuth (temporal) and range (spatial) correlation of the Ingara data set. The short term correlations in both range and azimuth were found to be shorter than those previously reported in the literature. This however may be attributed to the experimental conditions including high versus low grazing angles and flying versus stationary radar platforms. The analysis of the long-term correlations in Figures 15-16 shows that wavelengths of wind waves and swells may be retrievable from the range correlation whereas the periods of the wind waves and swells may also be recoverable from the azimuthal correlation.

In the same study, Dong [74] observed that the correlation between the HH and VV data were very low and the probability of high returns simultaneously measured by both the horizontally and vertically polarised antennas were significantly lower than that measured by just one. Utilising this property, he designed a CFAR scheme, which declares the presence of a target within a range bin only if both the HH and VV returns of the bin simultaneously exceed the respective HH and VV thresholds. This approach significantly reduced the false alarm rate.

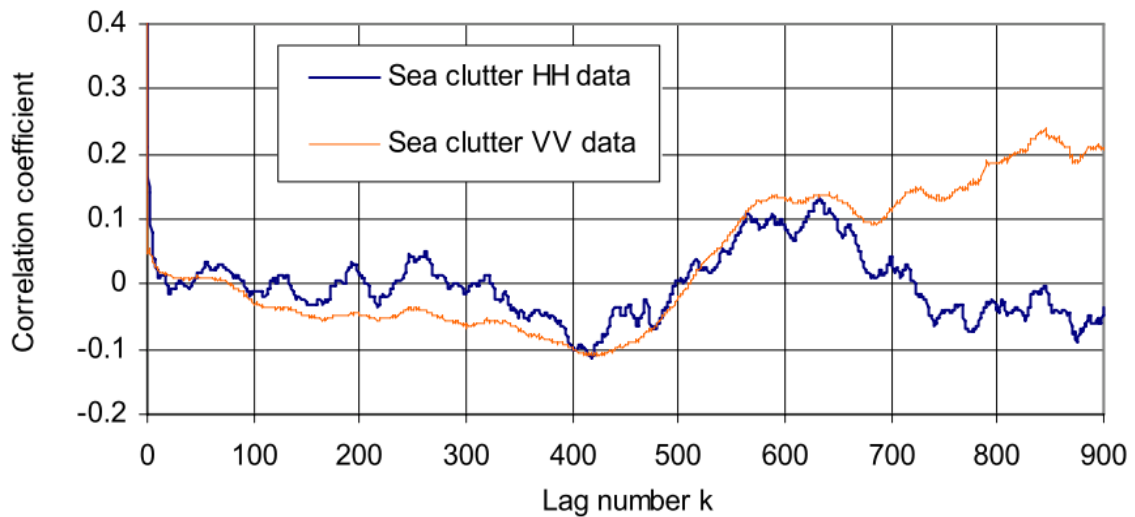


Figure 15: Range (spatial) correlation (reproduced from [74]).

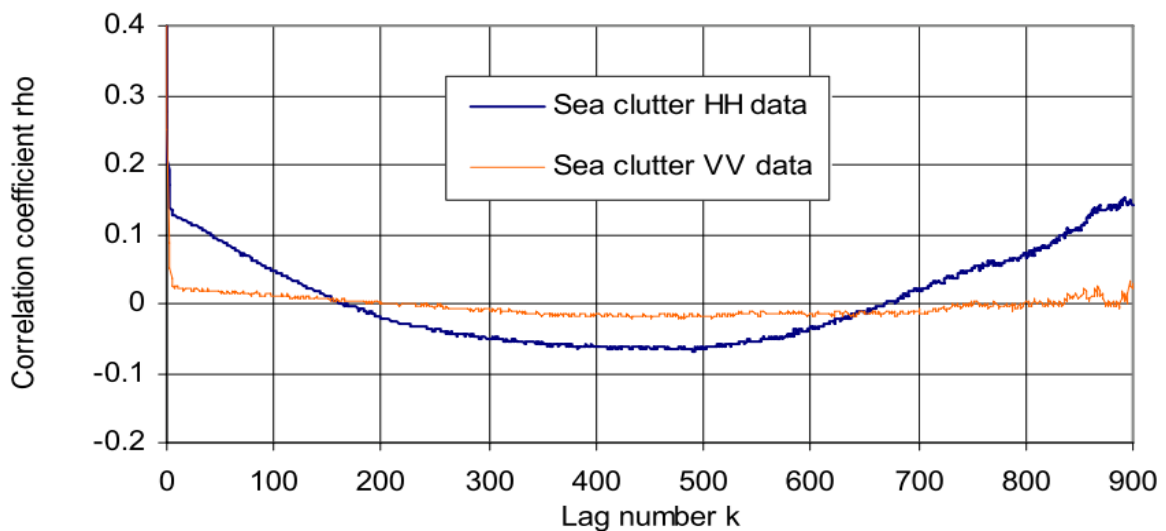


Figure 16: Azimuthal (temporal) correlation (reproduced from [74]).

6.4 Modelling and simulation of coherent sea-clutter

6.4.1 Models

The characteristics of high grazing angle sea-clutter can be represented by many of the modelling and simulation techniques that have been developed for low grazing angles.

The models for average reflectivity, σ^0 , are reasonably well established, as discussed in Section 4. Models for the amplitude statistics however, are still being developed. The literature discussed in Section 5 suggests that compound formulations, including the K distribution and its extensions to the KA and KK models, may be well suited for

representing high grazing angle sea-clutter [47, 59]. Other distributions, such as the Pareto distribution, are also being considered [63, 66]. These models still have limited application for performance prediction unless their parameters, particularly their shape, can be associated with the prevailing environmental conditions, the viewing geometry and radar characteristics. There are currently only a small number of parameter models [58] that are equivalent to those available for low grazing angle sea-clutter [38].

The least developed models, for both low and high grazing angle clutter, are those for Doppler spectra. In particular, it is known that in practice, clutter returns often exhibit non-stationary behaviour. This means that an average spectrum cannot fully represent the temporal or spatial evolution of clutter returns. It is known that clutter spikes may exhibit Doppler characteristics that are distinct from the main clutter returns (see Section 6.2) and that the spectra of the main clutter returns may vary in space and time, often correlated to some extent with the local clutter intensity, [68, 75]. Further work is needed to investigate the extent to which the model proposed in [68] can be applied more generally over a wide range of conditions, including high grazing angles. Comprehensive parameter models will also be needed to relate to these conditions.

These models can be further exploited to produce data for use in simulations. Appropriate methods are briefly reviewed below.

6.4.2 Simulation of amplitude statistics

The compound distribution models can be used to develop realistic simulations of clutter returns. In particular, the work by Tough and Ward [76] shows how to generate successive random variates that have a pre-determined amplitude distribution and autocorrelation function (ACF). In order to generate K distributed variates, the method in [76] is used to generate Gamma variates with a predefined shape parameter, ν , and ACF. These data are then used to modulate data with a random distribution representing the speckle component of the model. For non-coherent data, the speckle in the compound K distribution model will have a Rayleigh or exponential distribution (representing the amplitude and intensity, respectively). For coherent returns, the speckle component will have a complex Gaussian distribution. This Gaussian component may in turn have a Doppler spectrum, as discussed below.

6.4.3 Simulation of Doppler spectra

The standard compound K distribution model assumes that the local mean intensity (the Gamma distributed component) is constant over the typical dwell time of a radar processing interval. It is then quite straightforward to generate correlated complex Gaussian variates with a required spectrum or ACF. This approach is then sometimes extended on the assumption that the returns over time, with varying local intensity, can be treated as a Spherically Invariant Random Process (SIRP). However, such a model does not reproduce the non-stationary behaviour discussed above.

One approach to modelling this non-stationary behaviour is to assume that a spectrum can be used to represent the clutter over the dwell period, but that the spectrum characteristics

(mean Doppler shift, spectrum standard deviation, etc.) may then change over time or spatially. A model for this behaviour has been proposed in [68], based on observations of real radar data. This model represents the non-stationary behaviour as a mean Doppler shift of the spectrum that is a function of the local mean intensity, combined with random fluctuations of the spectrum standard deviation (spectrum width). This approach can be combined with a varying local mean intensity, generated by the methods described in [76], to produce a spectrum that varies over time and/or space. The increased non-Gaussian behaviour of the amplitude statistics at the edges of the spectrum, as observed over time or space at a given Doppler frequency, are well reproduced by this method. The method can be used to produce successive spectra, evolving over time. It is also possible to generate continuous time series data that exhibit the appropriate non-stationary behaviour.

Figure 17 shows a comparison of a spectrogram of real data and one of simulated data, designed using the methods described in [68] to have the same statistical characteristics as the real data.

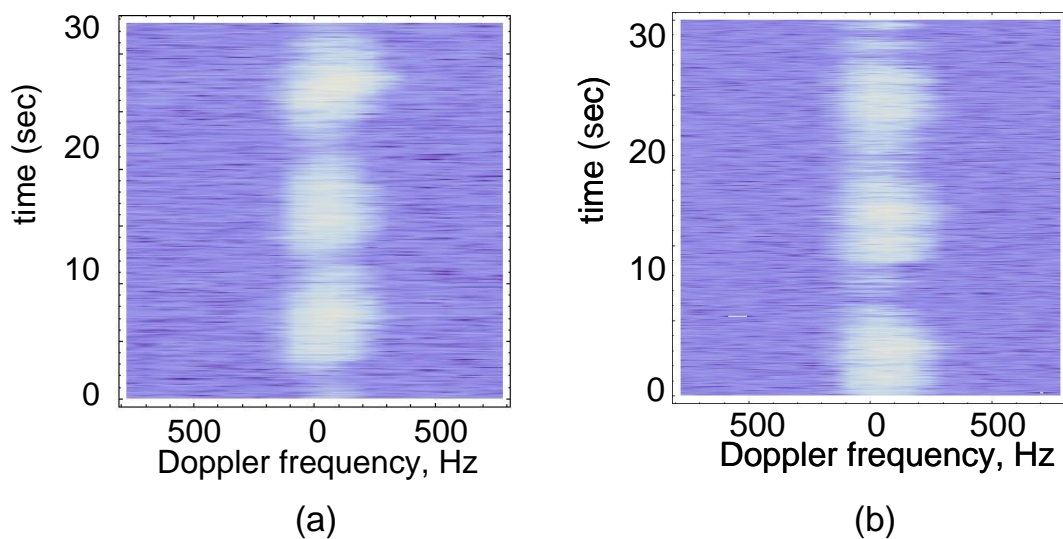


Figure 17: Doppler spectra comparison (dB) - (a) real data; (b) simulated spectra (reproduced from [68]).

7. Target Detection

Maritime target detection is a large area of research which has traditionally been focussed at low grazing angles. While there has not been a lot of work done specifically for high grazing angles, detection techniques have simply been developed using the amplitude distributions which have been found to accurately model high grazing angle sea-clutter. As described in Section 5, these are the K, KK and Pareto distributions.

The principal of target detection is shown in Figure 18, where two hypotheses can be defined, H_0 - clutter plus noise is present in the radar return and H_1 - a target is present with the clutter and noise. The premise of target detection is to select an acceptable probability of false alarm, P_{fa} and determine the constant false alarm rate (CFAR) threshold based on the clutter plus noise model. Any backscatter response above the CFAR threshold is then declared as a potential target.

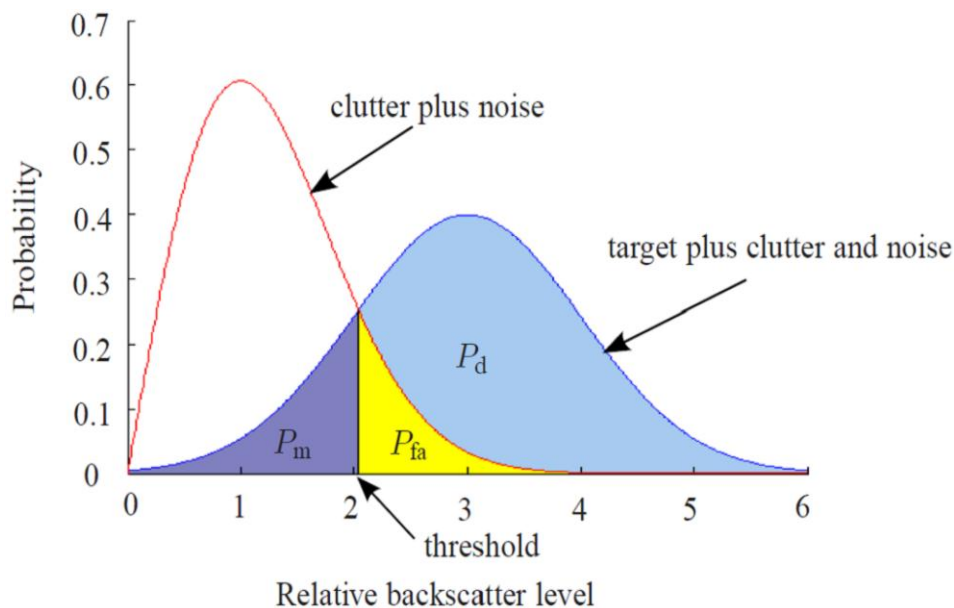


Figure 18: Target detection regions (reproduced from [77]).

This non-coherent target detection framework forms the basis of parametric modelling described in Section 7.1, which is concerned with estimating the mean behaviour of detecting a target in clutter and noise. The same hypothesis test can also be used to form optimal and sub-optimal coherent detectors. The relevant publications for this area are summarised in Section 7.2. The final Section 7.3 is concerned with utilising polarimetry for target detection from high grazing angles.

7.1 Parametric modelling

There have not been many studies concerned with target detection performance at high-grazing angles. By using the parameter models derived from the Ingara data [58], Rosenberg and Crisp [77] have compared the target detection performance for both constant and fluctuating targets using both K and KK clutter distributions. The mismatch in threshold between the K and KK distributions was demonstrated in Figure 12. If the incorrect threshold is used for target detection, the result is a significant mismatch in the required SIR for a given P_d . Detection probability results showed how stationary targets require a smaller SIR compared to fluctuating targets. Also, integrating over a number of pulses results in a smaller required SIR. Little difference was found with variation in azimuth, while higher grazing angles resulted in a significantly smaller required SIR.

A follow up study by Rosenberg [69] utilised the temporal correlation models from [72] to measure the effect of temporally correlated speckle. It was found that if the correlation is not accounted for, there is also a big mismatch in the required SIR for a given P_d . The results consistently found that the SIR difference between correlated and uncorrelated speckle for a P_{fa} of 10^{-6} was up to 4 dB for both the uncorrelated and correlated target models and that the SIR difference for the KK distribution was between 0.5-1.5 dB less than for the K distribution. An example is shown in Figure 19 for the three polarisation channels where the SIR difference is particularly high between the K and KK distributions for the HHH channel. Increasing the number of pulses or changing the polarisation channel did not significantly affect the SIR difference, while increasing the PRF or lowering the sea state increased the correlation and hence the SIR difference.

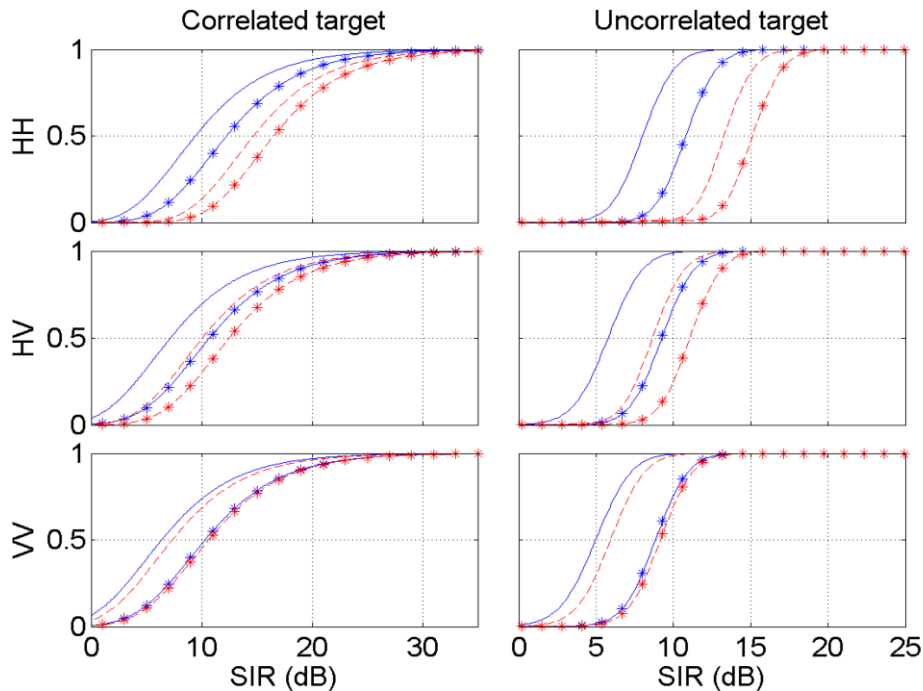


Figure 19: P_d variation with polarisation: (—) uncorrelated speckle (K), (---*) correlated speckle (K) (—) uncorrelated speckle (KK), (---*) correlated speckle (KK) (reproduced from [69]).

7.2 Optimal and sub-optimal detection

There has been a concentrated effort over the past few years to derive suitable optimal and sub-optimal, coherent detectors for use at high grazing angles. Weinberg has investigated optimal and sub-optimal coherent detectors using both the KK distribution [78, 79] and the Pareto distributions [80-83]. This work showed that the form of the optimal KK detector is extremely complicated and not feasible in a real radar system, while the optimal Pareto detector is far simpler. Also, for coherent multi-look detection in a Pareto clutter environment, the whitening matched filter detector which is optimal for Gaussian clutter, has been observed to perform very well as a sub-optimal detector. Recent work [84] has focussed on the development of constant false alarm rate detection processes for targets embedded within Pareto clutter. It was shown that a simple functional transform can produce such detection schemes, whose false alarm probability and threshold are related through simple analytic expressions. These relationships were also found to be intrinsically related to Gaussian detection counterparts.

7.3 Polarimetry

Early studies by Stacy et al. [45, 46] and Dong [74] have looked at characterising the polarimetric signature of high grazing angle sea-clutter. They used the Cloude-Pottier 'entropy-alpha' decomposition to determine the single and double bounce scatterers in the sea-clutter. Results in Figure 20 show that the distribution of high grazing angle sea-clutter spreads over a large portion of both the Bragg and non-Bragg regions, indicating that scattering mechanisms of sea-clutter are complex and multiple.

Dong's Mueller matrix decomposition [74] was developed to determine the relative contributions from double bounce, Bragg, odd bounce and cross scatterings for a given polarisation. It was also shown that the scattering mechanisms of the vertically polarised sea spikes are simpler than in the horizontal channel. Often, there is only one dominant scattering mechanism with the VV spikes, whereas the HH spikes are more complex with multiple scatterers often contributing to the radar return. Analysis of a C-band polarimetric synthetic aperture radar showed that while the sea surface is dominated by Bragg scattering, the test vessels as well as urban areas were dominated by the double and odd bounce scattering mechanisms. Similar results were also found by Crisp et al. [85] who looked at a wooden fishing boat using the Ingara radar. Results shown in Figure 21 from an example target indicates that HH, cross-slant 45° and right hand circular transmit / receive (RR) are the best polarisations for detecting targets.

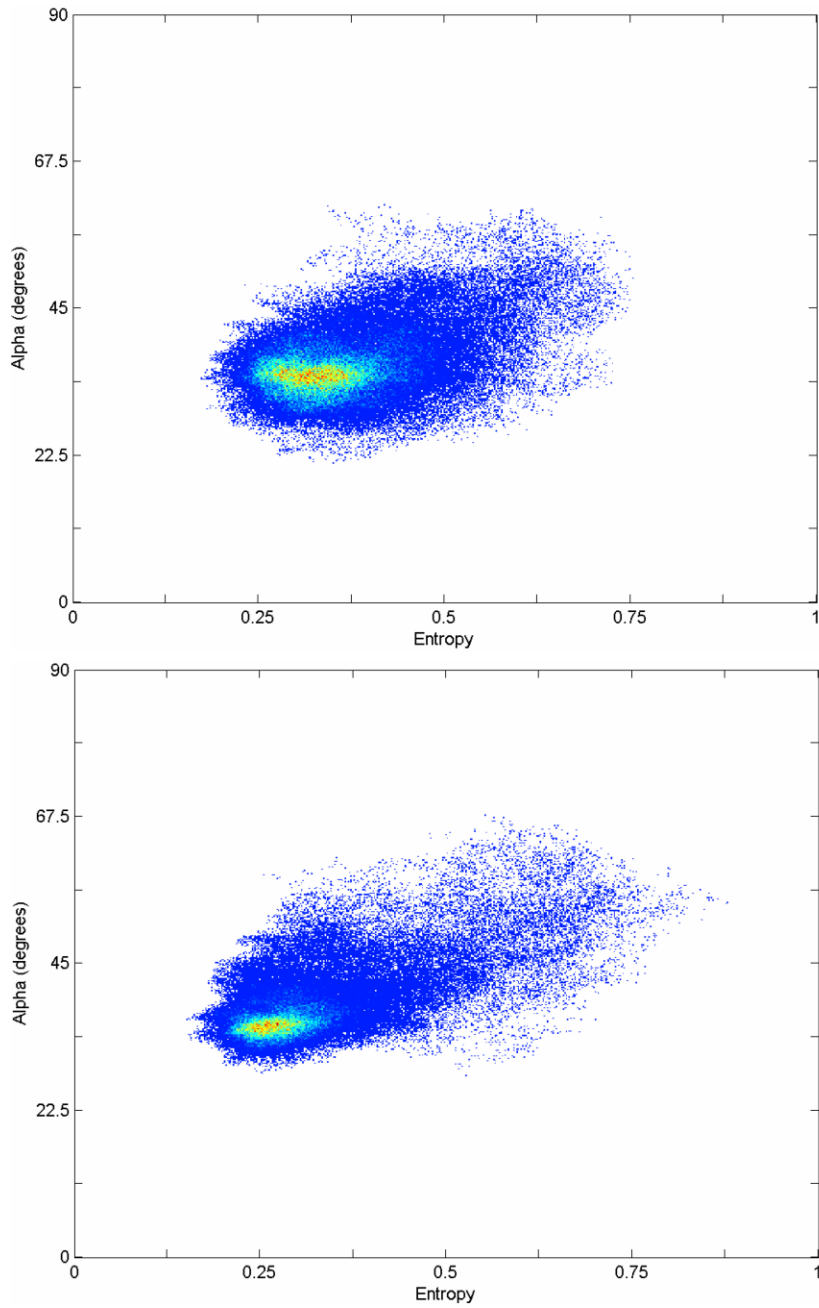


Figure 20: The Cloude-Pottier entropy-alpha angle scatter plots for the (top) upwind and (bottom) downwind imaging geometries (reproduced from [45]).

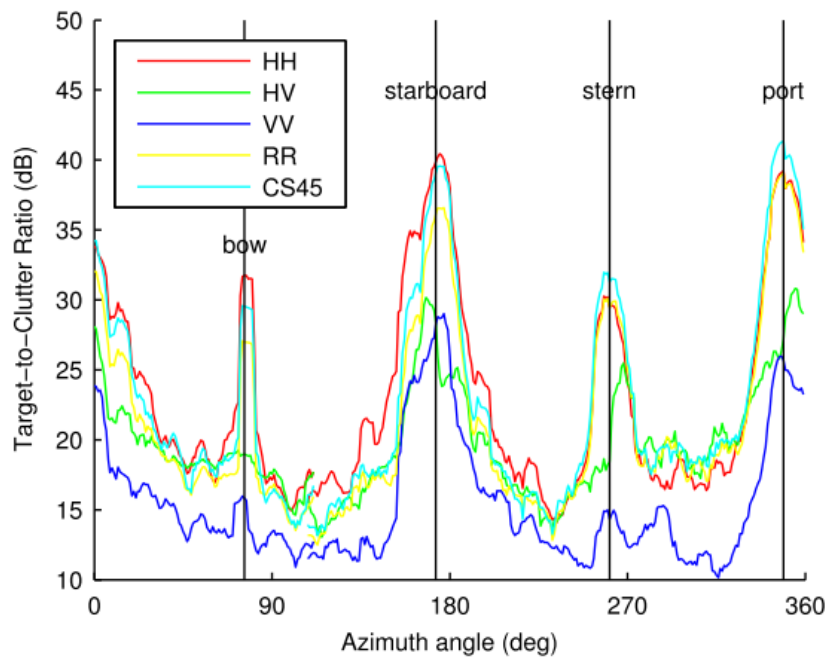


Figure 21: Variation with respect to polarisation and azimuth angle of the target to clutter ratio at 40° grazing (reproduced from [85]).

8. Conclusions

This report has summarized the current literature on high grazing angle sea-clutter. A study of the relevant physics of the scattering was first covered, followed by a summary of experiments that have been conducted at high grazing angles. A large number of relevant areas were then covered including the mean backscatter, amplitude statistics, the Doppler spectrum and correlation and target detection.

It should be noted that all of the data is unanimous in showing a monotonic increase in the mean backscatter with increasing grazing angle. It has also been reported that while high grazing angle sea-clutter is less spiky than at low grazing angles, the amplitude statistics still have significantly non-Gaussian characteristics. The Doppler spectra of sea-clutter is also highly variable, again reflecting the presence of discrete spikes as well as the more dominant Bragg scattering components. These factors combined with an enlarged clutter cell size, implies that detection of small targets will likely become harder as the grazing angle increases.

Further measurements representative of a wide range of environmental conditions are required to develop robust models, especially for amplitude statistics and Doppler spectra. These will assist the assessment and development of signal processing methods required to detect difficult targets when operating from airborne platforms at high grazing angles.

References

- [1] Technology Service Corporation, *Backscatter from sea*. Radar Workstation, 1990. **2**: p. 177-186.
- [2] Crisp, D.J., R. Kyprianou, L. Rosenberg, and N.J. Stacy, *Modelling the mean ocean backscatter coefficient in the plateau region at X-band*. Research report DSTO-RR-0383, DSTO, 2012.
- [3] Rosenberg, L., *Characterisation of Medium Grazing Angle X-band Sea-clutter Doppler Spectra from an Airborne Platform*. Research Report In preparation, DSTO, 2012.
- [4] Rice, D.O., *Reflections of electromagnetic waves from slightly rough surfaces*. Communications on Pure and Applied Maths, 1951. **4**: p. 361-378.
- [5] Peake, W.H. *Theory of radar return from terrain*. IRE Convention Record, 1959.
- [6] Wright, J.W., *Backscattering from capillary waves with application to sea clutter*. IEEE Transactions on Antennas and Propagation, 1966. **AP-14**(6): p. 749-754.
- [7] Wright, J.W., *A new model for sea clutter*. IEEE Transactions on Antennas and Propagation, 1968. **16**(2): p. 217-223.
- [8] Ulaby, F.T., R.K. Moore, and A.K. Fung, *Microwave Remote Sensing: Active and Passive, Volume II: Radar Remote Sensing and Surface Scattering and Emission Theory*. 1982: Addison-Wesley.
- [9] Wetzel, L.B., *Radar Handbook*, M.I. Skolnik, Editor. 2008, McGraw-Hill.
- [10] Guinard, N.W. and J.C. Daley, *An experimental study of a sea clutter model*. Proceedings of the IEEE, 1970. **58**: p. 543-550.
- [11] Valenzuela, G.R., M.B. Laing, and J.C. Daley, *Ocean spectra for the high-frequency waves as determined from airborne radar measurements*. Journal of Marine Research, 1971. **29**: p. 69-84.
- [12] Bass, F.G., I.M. Fuks, A.I. Kalmykov, I.E. Ostrovsky, and A.D. Rosenberg, *Very High Frequency Radiowave scattering by a distributed sea surface, Part II: scattering from an actual sea surface*. IEEE Transactions on Antennas and Propagation, 1968. **16**(5): p. 560-568.
- [13] Hasselmann, K. and M. Schieler. *Radar backscatter from the sea surface*. Symposium on Naval Hydrodynamics, 1970.
- [14] Valenzuela, G.R. and M.B. Laing, *Study of Doppler spectra of radar sea echo*. Journal of Geophysical Research, 1970. **75**: p. 551-563.
- [15] Hicks, N.L., N. Knable, J.J. Kovaly, G.S. Newell, J.P. Ruina, and C.W. Sherwin, *The Spectrum of X-band radiation backscattered from the sea surface*. Journal of Geophysical Research, 1960. **65**(3): p. 825-837.
- [16] Pidgeon, V.W., *Doppler dependence of radar sea return*. Journal of Geophysical Research, 1968. **73**(4): p. 1333-1341.
- [17] Money, D.G., A. Mabogunje, D. Webb, and M. Hooker, *Sea Clutter Power Spectral Lineshape Measurements*, in *IEEE Radar Conference*. 1997.
- [18] Duncan, J.R., W.C. Keller, and J.W. Wright, *Fetch and wind speed dependence of Doppler spectra*. Radio Science, 1974. **9**: p. 809-819.
- [19] Rozenberg, A.D., D.C. Quigley, and W.K. Melville, *Laboratory study of polarized scattering by surface waves at grazing incidence: The influence of long waves*. IEEE Transactions on Geoscience and Remote Sensing, 1996. **34**(6): p. 1331-1342.

- [20] Lee, P.H.Y., J.D. Barter, K.L. Beach, C.L. Hindman, B.M. Lake, H. Rungaldier, J.C. Shelton, A.B. Williams, R. Yee, and H.C. Yuen, *X-band microwave backscattering from ocean waves*. Journal of Geophysical Research, 1995. **100**(C2): p. 2591-2611.
- [21] Kalmykov, A.I. and V.V. Pustovoytenko, *On polarization features of radio signals scattered from the sea surface at small grazing angles*. Journal of Geophysical Research, 1976. **81**(C12): p. 1960-1964.
- [22] Lewis, R.L. and I.D. Olin, *Experimental study and theoretical model of high resolution backscatter from the sea-clutter*. Radio Science, 1980. **15**: p. 815-826.
- [23] Lyzenga, D.R., A.L. Maffett, and R.A. Shuchman, *The contribution of wedge scattering to the radar cross section of the ocean surface*. IEEE Transactions of Geoscience and Remote Sensing, 1983. **GE-21**(4): p. 502-505.
- [24] Plant, W.J., *A model for microwave Doppler sea return at high incidence angles: Bragg scattering from bound, tilted waves*. Journal of Geophysical Research, 1997. **102**(C9): p. 21,131-21,146.
- [25] Jessup, A.T., W.K. Melville, and W.C. Keller, *Breaking Waves affecting Microwave Backscatter, 1. Detection and Verification*. Journal of Geophysical Research, 1991. **96**(C11): p. 20,547-20,559.
- [26] Jessup, A.T., W.K. Melville, and W.C. Keller, *Breaking Waves affecting Microwave Backscatter, 2. Dependence on wind and wave conditions*. Journal of Geophysical Research, 1991. **96**(C11): p. 20,561-20,569.
- [27] Werle, B.O. *Sea Backscatter, spikes and wave group observations at low grazing angles*. IEEE International Radar Conference, 1995.
- [28] Keller, M.R., B.L. Gotwols, and R.D. Chapman. *Multiple sea spike definitions: reducing the clutter*. IEEE International Geoscience and Remote Sensing Symposium, 2002.
- [29] Melief, H.W., H. Greidanus, van Genderen, P., and P. Hoogeboom, *Analysis of sea spikes in radar sea clutter data*. IEEE Transactions on Geoscience and Remote Sensing, 2006. **44**(4): p. 985-993.
- [30] Long, M.W., *Radar Reflectivity of Land and Sea - Third Edition*. 2001: Artech House.
- [31] Walker, D., *Doppler modelling of radar sea clutter*. IEE Proceedings of Radar, Sonar and Navigation, 2001. **148**(2): p. 73-80.
- [32] Trizna, D.B., *A model for Brewster angle damping and multipath effects on the microwave radar sea echo at low grazing angles*. IEEE Transactions on Geoscience and Remote Sensing, 1997. **35**(5): p. 1232-1244.
- [33] Sletten, M.A., D.B. Trizna, and J.P. Hansen, *Ultrawide-band radar observations of multipath propagation over the sea surface*. IEEE Transactions on Antennas and Propagation, 1996. **44**(5): p. 646-651.
- [34] World Meteorological Organization, *Guide to Wave Analysis and Forecasting*. WMO-No.702, 1998.
- [35] Tucker, M. and E. Pitt, *Waves in Ocean Engineering*. 2001: Elsevier Ocean Engineering Series.
- [36] Nathanson, F.E., J.P. Reilly, and M.N. Cohen, *Radar Design Principles - Second Edition*. 1991: McGraw-Hill.
- [37] Fairbridge, R.W., *Encyclopedia of Oceanography*. 1966: Van Nostrand Reinhold Company.
- [38] Ward, K.D., R.J.A. Tough, and S. Watts, *Sea Clutter: Scattering, the K-Distribution and Radar Performance*. 2006: The Institute of Engineering Technology.

- [39] Kwoh, D.S.W. and B.M. Lake. *The nature of microwave backscattering from water waves*. NATO/ AGARD Conference Proceedings, 1983.
- [40] Melville, W.K., A.D. Rozenberg, and D.C. Quigley. *Laboratory study of polarized microwave scattering at grazing incidence*. IEEE International Geoscience and Remote Sensing Symposium, 1995.
- [41] Lee, P.H.Y., J.D. Barter, E. Caponi, C.L. Hidman, B.M. Lake, and H. Rungaldier, *Wind-speed dependence of small-grazing-angle microwave backscatter from sea surfaces*. IEEE Transactions on Antennas and Propagation, 1996. **44**(3): p. 333-340.
- [42] Rozenberg, A., D. Quigley, M. Ritter, and W.K. Melville. *Laboratory study of polarized microwave scattering from steep waves at grazing incidence*. IEEE International Geoscience and Remote Sensing Symposium, 1997.
- [43] Lamont-Smith, T., *Investigation of the variability of Doppler spectra with radar frequency and grazing angle*. IEE Proceedings of Radar, Sonar and Navigation, 2004. **151**(5): p. 291-298.
- [44] Masuko, H., K. Okamoto, M. Shimada, and S. Niwa, *Measurement of Microwave Backscattering Signatures of the Ocean Surface Using X Band and Ka Band Airborne Scatterometers*. Geophysical Research, 1986. **91**(C11): p. 13065-13083.
- [45] Stacy, N.J.S., D. Crisp, A. Goh, D. Badger, and M. Preiss. *Polarimetric Analysis of Fine Resolution X-Band SAR Sea Clutter*. IEEE International Conference on Geoscience and Remote Sensing Symposium, 2005.
- [46] Stacy, N.J.S., M. Preiss, and D. Crisp. *Polarimetric Charactersitics of X-Band SAR Sea Clutter*. IEEE International Conference on Geoscience and Remote Sensing Symposium, 2006.
- [47] Dong, Y., *Distribution of X-Band High Resolution and High Grazing Angle Sea Clutter*. Research Report DSTO-RR-0316, DSTO, 2006.
- [48] Stacy, N.J.S., D.P. Badger, A.S. Goh, M. Preiss, and M.L. Williams. *The DSTO Ingara airborne X-Band SAR polarimetric upgrade: first results*. IEEE International Geoscience and Remote Sensing Symposium, 2003.
- [49] Reilly, J.P., *Clutter models for shipboard radar applications, 0.5 to 70 GHz, multi-sensor propagation data and clutter modelling*. F2A-88-0-307R2, NAAW-88-062R2 Technical Report Task 3-1-18, NATO AAW System Program Office, 1998.
- [50] Branson, J., S. Billett, H. Neil, and W. Will, *Naval Environmental Clutter, Attenuation and Propagation Specification - NECAPS 4.1*. QinetiQ/D&TS/SEA/TS0700336/2.1, QinetiQ, 2011.
- [51] Gregers-Hansen, V. and R. Mittal, *An improved empirical model for radar sea clutter reflectivity*. IEEE Transaction on Aerospace and Electronic Systems, 2012. **48**(4): p. 3512-3524.
- [52] Crisp, D.J., R. Kyprianou, L. Rosenberg, and N.J. Stacy. *Modelling X-Band Sea Clutter at Moderate Grazing Angles*. IEEE International Radar Conference, 2008.
- [53] Macdonald, F.C. *The correlation of radar sea clutter on vertical and horizontal polarization with wave height and slope*. IRE International Convention, 1956.
- [54] Horst, M.M., F.B. Dyer, and M.T. Tuley. *Radar Sea Clutter Model*. IEEE International Conference of Antennas and Proagation, 1978.
- [55] Beckmann, P., *The Scattering of Electromagnetic Waves from Rough Surfaces*. 1963: Pergamon Press Ltd.
- [56] Spaulding, B., D. Horton, and H. Pham. *Wind Aspect Factor in Sea Clutter Modeling*. IEEE International Radar Conference, 2005.

- [57] Rosenberg, L., D.J. Crisp, and N.J. Stacy. *Analysis of the KK-Distribution with X-band Medium Grazing Angle Sea-Clutter*. IEEE International Radar Conference, 2009.
- [58] Rosenberg, L., D.J. Crisp, and N.J. Stacy. *Statistical Models for Medium Grazing Angle X-band Sea-Clutter*. Defence Applications of Signal Processing, 2009.
- [59] Rosenberg, L., D.J. Crisp, and N.J. Stacy, *Analysis of the KK-Distribution with Medium Grazing Angle Sea-clutter*. IET Proceedings of Radar Sonar and Navigation, 2010. **4**(2): p. 209-222.
- [60] Crisp, D.J., L. Rosenberg, N.J. Stacy, and Y. Dong. *Modelling X-band Sea-Clutter with the K-distribution: Shape Parameter Variation*. IEEE International Radar Conference, 2009.
- [61] Dong, Y. and B. Haywood. *High Grazing Angle X-band Sea clutter Distributions*. IET International Radar Conference, 2007.
- [62] Weinberg, G.V., *An Investigation of the Pareto Distribution as a Model for High Grazing Angle Clutter*. Technical Report DSTO-TR-2525, DSTO, 2011.
- [63] Weinberg, G.V., *Assessing Pareto fit to high-resolution high-grazing-angle sea clutter*. IET Electronic Letters, 2011. **47**(8): p. 516-517.
- [64] Weinberg, G.V. and D. Finch, *Analysis of a Pareto Mixture Distribution for Maritime Surveillance Radar*. Journal of Electrical and Computer Engineering, 2012. **2012**.
- [65] Rosenberg, L. *Persistent Sea-spike Detection in Medium Grazing Angle X-band Sea-clutter*. European SAR conference, 2012.
- [66] Rosenberg, L. and S. Bocquet. *Pareto Distribution Models for High Grazing Angle X-band Sea-Clutter*. Submitted to IEEE Proceedings on Geoscience and Remote Sensing, 2013.
- [67] Rosenberg, L. *The effect of temporal correlation with K and KK-distributed Sea-Clutter*. IEEE Radarcon Conference, 2012.
- [68] Watts, S., *Modeling and Simulation of Coherent Sea Clutter*. IEEE Transaction on Aerospace and Electronic Systems, 2012. **48**(4): p. 3303-3317.
- [69] Rosenberg, L., D.J. Crisp, and N.J. Stacy. *Characterisation of Low-PRF X-band Sea-clutter Doppler Spectra*. IEEE International Radar Conference, 2008.
- [70] Rosenberg, L. and N.J. Stacy. *Analysis of Medium Angle X-band Sea-clutter Doppler Spectra*. IEEE Radarcon Conference, 2008.
- [71] Walker, D., *Experimentally Motivated Model for Low Grazing Angle Radar Doppler Spectra of the Sea Surface at Small Grazing Angles*. IEE Proceedings of Radar, Sonar and Navigation, 2000. **147**(3): p. 114-121.
- [72] Rosenberg, L., *Characterisation of Medium Grazing Angle X-band Sea-clutter Doppler Spectra from an Airborne Platform*. Submitted to IEEE Transaction on Aerospace and Electronic Systems, 2013.
- [73] Proakis, J.G. and D.G. Manolakis, *Digital Signal Processing Principles, Algorithms and Applications - Third Edition*. 1996: Prentice-Hall, Inc.
- [74] Dong, Y., *High Grazing Angle and High Resolution Sea-clutter: Correlation and Polarisation Analyses*. Research Report DSTO-RR-1972, DSTO, 2007.
- [75] Greco, M., F. Bordonì, and F. Gini, *X-band Sea-clutter nonstationary: influence of long waves*. IEEE Journal of Oceanic Engineering, 2004. **29**(2): p. 269-293.
- [76] Tough, R.J.A. and K.D. Ward, *The correlation properties of gamma and other non-Gaussian processes generated by memoryless nonlinear transformation*. Journal of Applied Physics, 1999. **32**: p. 3075-3084.

- [77] Rosenberg, L. and D. Crisp. *X-band Performance with Medium Grazing Angle Sea-Clutter*. European SAR Conference, 2010.
- [78] Weinberg, G.V., *Coherent Multilook Radar Detection for Targets in KK Distributed Clutter*. 2012, InTech. p. 161-176.
- [79] Weinberg, G.V., *Suboptimal Coherent Radar Detection in a KK-Distributed Clutter Environment*. ISRN Signal Processing, 2012. **2012**.
- [80] Weinberg, G.V., *Coherent Multilook Radar Detection for Targets in Pareto Distributed Clutter*. Technical Report DSTO-TR-2646, DSTO, 2012.
- [81] Weinberg, G.V., *Validity of whitening-matched filter approximation to the Pareto coherent detector*. IET Signal Processing, 2012. **6**(6): p. 546-550.
- [82] Weinberg, G.V., *Coherent multilook detection for targets in Pareto distributed clutter*. IET Electronic Letters, 2011. **47**(14): p. 822-824.
- [83] Weinberg, G.V., *Assessing Detector Performance with Application to Pareto Coherent Multilook Radar Detection*. IET Radar Sonar and Navigation, 2013.
- [84] Weinberg, G.V., *CFAR Detectors for Pareto Clutter Models*. Submitted to IET Radar Sonar and Navigation, 2013.
- [85] Crisp, D.J., N.J.S. Stacy, D.A. Hudson, P.B. Pincus, and A.S. Goh. *Polarimetric Analysis of Maritime SAR Data Collected with the DSTO Ingara X-Band Radar*. IEEE Geoscience and Remote Sensing Conference, 2007.

DEFENCE SCIENCE AND TECHNOLOGY ORGANISATION DOCUMENT CONTROL DATA					
				1. PRIVACY MARKING/CAVEAT (OF DOCUMENT)	
2. TITLE High Grazing Angle Sea-Clutter Literature Review			3. SECURITY CLASSIFICATION (FOR UNCLASSIFIED REPORTS THAT ARE LIMITED RELEASE USE (L) NEXT TO DOCUMENT CLASSIFICATION) <div style="display: flex; justify-content: space-between;"> Document (U) </div> <div style="display: flex; justify-content: space-between;"> Title (U) </div> <div style="display: flex; justify-content: space-between;"> Abstract (U) </div>		
4. AUTHOR(S) Luke Rosenberg and Simon Watts			5. CORPORATE AUTHOR DSTO Defence Science and Technology Organisation PO Box 1500 Edinburgh South Australia 5111 Australia		
6a. DSTO NUMBER DSTO-GD-0736		6b. AR NUMBER AR-015-559		6c. TYPE OF REPORT General Document	
				7. DOCUMENT DATE March 2013	
8. FILE NUMBER 2013/1007152/1		9. TASK NUMBER AIR7000		10. TASK SPONSOR DGAD	
				11. NO. OF PAGES 44	
				12. NO. OF REFERENCES 85	
13. DSTO Publications Repository http://dspace.dsto.defence.gov.au/dspace/				14. RELEASE AUTHORITY Chief, Electronic Warfare and Radar Division	
15. SECONDARY RELEASE STATEMENT OF THIS DOCUMENT <p style="text-align: center;"><i>Approved for public release</i></p> <p>OVERSEAS ENQUIRIES OUTSIDE STATED LIMITATIONS SHOULD BE REFERRED THROUGH DOCUMENT EXCHANGE, PO BOX 1500, EDINBURGH, SA 5111</p>					
16. DELIBERATE ANNOUNCEMENT No Limitations					
17. CITATION IN OTHER DOCUMENTS No Limitations					
18. DSTO RESEARCH LIBRARY THESAURUS Radar, sea-clutter, high grazing angle, literature review					
19. ABSTRACT This report reviews the published literature on the characteristics of mono-static radar sea-clutter observed with high grazing angles (typically above about 10°). To date, most of the analysis and modelling of sea-clutter has been undertaken at low grazing angles with the main application being for surface and airborne maritime radars. The report identifies some of the data sets that have been collected and the empirical models that have been developed from them for the normalised radar cross-section. The amplitude statistics and Doppler spectra of high grazing angle clutter are reviewed and the implications for radar design and target detection are discussed.					